

20170727: DARK MATTER SEARCH AND ELECTRON BACKGROUND
EVALUATION
TESTING OF TPC GRID DESIGNING

A DISSERTATION
SUBMITTED TO THE DEPARTMENT OF PHYSICS
AND THE COMMITTEE ON GRADUATE STUDIES
OF STANFORD UNIVERSITY
IN PARTIAL FULFILLMENT OF THE REQUIREMENTS
FOR THE DEGREE OF
DOCTOR OF PHILOSOPHY

Wei Ji
June 2018

© Copyright by Wei Ji 2018
All Rights Reserved

I certify that I have read this dissertation and that, in my opinion, it is fully adequate in scope and quality as a dissertation for the degree of Doctor of Philosophy.

(Tom Shutt) Principal Adviser

I certify that I have read this dissertation and that, in my opinion, it is fully adequate in scope and quality as a dissertation for the degree of Doctor of Philosophy.

(Dan Akerib)

I certify that I have read this dissertation and that, in my opinion, it is fully adequate in scope and quality as a dissertation for the degree of Doctor of Philosophy.

(Peter Graham)

I certify that I have read this dissertation and that, in my opinion, it is fully adequate in scope and quality as a dissertation for the degree of Doctor of Philosophy.

(Giorgio Gratta)

I certify that I have read this dissertation and that, in my opinion, it is fully adequate in scope and quality as a dissertation for the degree of Doctor of Philosophy.

()

Approved for the Stanford University Committee on Graduate Studies

Preface

This thesis is discussing about the design and validation of liquid xenon LZ Dark Matter experiment and results from LUX Dark Matter experiment.

Acknowledgments

I would like to thank...

Contents

Preface	v
Acknowledgments	vi
List of Tables	viii
List of Figures	ix
1 Introduction to Time Projection Chamber.	1
1.1 Introduction	2
1.2 Time Projection Chamber	2
1.2.1 light, charge, heat	2
1.2.2 Initial state	2
1.2.3 S1 light	2
1.2.4 electron drift	2
1.2.5 S2 light	2
1.2.6 ion drift	2
1.2.7 heat	2
1.2.8	2
1.3 Liquid Noble Gas TPCs	2
1.3.1 Liquid Xenon detectors	2
1.3.2 Liquid Argon detectors	2
1.3.3 Other Gaseous Noble element detectors	2
1.4 Photon and electron detection	2
1.5 Gaseous noble gas detector	2
1.5.1 Particle transportation	2
1.5.2 Particle energy deposition	2
1.5.3 Position reconstruction	2
1.5.4 Energy reconstruction	3

1.5.5	Particle transportation	3
1.5.6	Particle energy deposition	3
1.5.7	Position reconstruction	3
1.5.8	Energy reconstruction	3
2	Grid Design in detectors.	4
2.1	Parallel Wire	4
2.2	woven wire	4
2.3	etched grid of different shape	4
2.4	electron emission on grid wires	4
2.5	secondary electron from grid wires	4
2.6	Material	4
3	Electron emission in LUX Detector, and LZ Prototype System Test	5
3.1	LUX	5
3.2	LZ Prototype System test phase I	5
3.3	LZ GAS TEST	5
3.4	LZ	5
4	other electron and photon sources and sink in liquid xenon detector	6
4.1	electron sink	6
4.2	electron source	6
4.3	light sink	6
4.4	light source	6
4.5	light scattering	6
4.6	secondary electron after S1	7
4.7	secondary electron after S2	7
4.8	s	7
5	Electron measurement and dark matter	8
5.1	electron recoil background	8
5.2	leptonphilic model dark matter	8
5.3	sub-GeV, small S2 dark matter	8
5.4	double beta decay	8
6	More about gaseous noble gas detector	9
6.1	Introduction	9
6.1.1	S2	9
6.1.2	ionization	9

6.2	emission process on cathode	9
6.2.1	Surface field induced first emission	9
6.2.2	Photoelectric effect	9
6.2.3	ion-induced and metastable particle induced effect	9
6.3	breakdown in gas and liquid	9
6.3.1	stream breakdown	9
6.3.2	townsend breakdown	9
7	Production and propagation of photon and electron signals in argon and xenon TPC	10
7.1	Mean Free Path	11
7.2	Energy deposition of an event in argon and xenon	11
8	Metal in detector	13
8.1	Metal in Vacuum	13
8.1.1	I-V curves	13
8.1.2	Fowler-Nordheim Plot and Surface factor	13
8.1.3	Shortkey Barier and	13
8.2	Metal in Liquid	13
8.2.1	Band Structure	13
8.2.2	Liquid "Work Function"	13
8.2.3	13
8.3	Treatment of Stainless to reduce emission	13
8.3.1	polishing, passivation, gas conditioning	13
9	Gas phase xenon detector for wire testing	15
9.1	The gas phase xenon detector	16
9.1.1	The Chamber	16
9.1.2	Test Mass	16
9.1.3	DAQ system.	16
9.1.4	External trigger	16
9.1.5	High voltage feed through and inside outside cable connectors	16
9.1.6	Gas circulation system	16
9.2	Sparking in the system	17
9.2.1	The sparking on the high voltage feed through connectors	18
9.2.2	The sparking on the cable grounding terminations	18
9.2.3	The sparking between the grids	18
9.3	Light propagation Simulations	18

9.3.1	Light creation	18
9.3.2	Light collection efficiency	20
9.4	DAQ configuration, DAQ dead time and Required silence pre-trigger	20
9.5	Data processing	20
9.6	PMT single photo electron area calibration	20
9.7	Understanding of the events	20
9.8	Drift velocity calibration	23
9.9	Electron emission changing over time	24
9.10	The influence of impurity in xenon	24
9.11	The influence of long operation duration	24
9.12	The influence of grid passivations	24
9.13	Discussion about LZ grids	24
10	EFT/IDM WIMP search with LUX	45
10.1	Run stability	45
10.1.1	General	46
10.1.2	PMT	46
10.1.3	Light yield	46
10.1.4	Exposure time	46
10.1.5	16 separate detectors	47
10.1.6	Summary	47
10.2	Cut and cut efficiency	47
11	Overview of Dark Matter research	48
11.1	Cosmological evidence for dark matter	49
11.1.1	Evolution of the universe, density perturbation	49
11.1.2	Nucleosynthesis	50
11.1.3	The Cosmic Microwave Background	52
11.1.4	Structure formation	54
11.2	Galactic Evidence of dark matter	55
11.2.1	Galactic Rotation Curves	55
11.3	Other Observations	56
11.4	Evidence of Dark Matter	56
11.4.1	56
11.4.2	Gravitational lensing	56
11.4.3	Dark matter in clusters, galaxies	56
11.5	Dark matter candidates	56
11.5.1	Neutrinos	56

11.5.2	macho,super massive blackholes	56
11.5.3	WIMP	56
12	Future overview of experiments for Dark Matter detection	57
12.1	LZ	58
12.1.1	58
12.1.2	58
12.2	Xenon100, Xenon-nT	58
12.2.1	58
12.2.2	58
12.3	DarkSide-50, DarkSide-20k	58
12.3.1	58
12.3.2	58
12.4	EXO, EXO200, nEXO	58
12.4.1	58
12.4.2	58
12.5	Other Liquid Xenon experiments, xmass,	58
12.5.1	58
12.5.2	58
12.6	Other Liquid Argon TPC Experiments, miniclean, microboon, etc	58
12.6.1	58
12.6.2	58
12.7	NEXT	58
12.7.1	58
12.7.2	58
13	candidates and direct detection	59
14	<i>Gas Test</i> descriptions	60
14.1	DAQ	60
14.2	Cuts	60
14.2.1	Summary of the cuts	61
15	<i>Gas Test</i> result	62
A	Calculation of voltage distribution in TPC	63
A.1	Parallel-component detectors	63
A.1.1	A single grid plane	66
A.1.2	A meshed grid plane	68

A.1.3 etched grid with triangle, square or hexagon pattern	69
A.2 Deflection of the grid plane	71
B Error propagation discussion	77
B.1 Bernoulli(Binomial) Process	77
B.2 Multiplication Process	78
C Binomial likelihood discussion	81
D Cryogenic and flow system in liquid xenon detector	83
D.1 Thermosyphon	83
D.2 heater PID	83
D.3 Heat exchanger	83
D.4 circulation system	83
D.5 wave	83
D.6 bubble	83
E Sensors	84
E.1 Level sensors	84
E.1.1 Differential pressure	84
E.1.2 Capacitance	85
E.2 Temperature sensor	87
F Gas Test RQ list	92
G Abbreviations	98
Bibliography	100

List of Tables

9.1	Spectral response of the PMTs tested in HAMAMATSU	17
9.2	PMT areas calibration.	20
F.1	RQ list	97

List of Figures

8.1 [5]	14
9.1 Top: The Gas Detector without the outer vessel. Bottom: The Gas Detector with the outer vessel assembled. On top of the deck is the electronic and gas gauge breakouts. On the right is the vacuum pumping system.	25
9.2 Left: one PMT setup. Right: two PMT setup.	26
9.3 Top left: the amplifier. Bottom left: the digitizer. Right: the back side of the Gas Detector.	26
9.4 External trigger system	27
9.5 Top: ceramic feed through. Middle: external filter boxes. Bottom: internal cables and connectors.	28
9.6 Top left: KNF circulation pump. Middle left: storage bottles. Top right: the gas circulation panel. Bottom: the gas circulation panel Piping and Instrumentation Diagram (P&ID)	29
9.7 Fluorescence light from the PTFE surface decaying with time	29
9.8 The number of photons created per electron between the anode grid and the gate grid. A 13mm gap size is assumed.	30
9.9 Light collection efficiency(PDE) inside the detector region between anode grid and gate grid(simulated with PTFE reflectivity of 0.40). Top: light collection efficiency vs radius from the center of the grid ring at different location. Blue: 2 mm above the gate grid. Red: in the middle between the anode grid and the gate grid. Yellow: 2 mm below the anode grid. Middle: top and bottom PMT light collection efficiency. Blue: top PMT. Red: bottom PMT. Yellow: total. Bottom: light collection efficiency in the middle between the anode grid and the gate grid. Red solid curve is the region of the grid wires.	31
9.10 Light collection efficiency inside the detector region rz cross section (simulated with PTFE reflectivity of 0.40). Top: top PMT only. Middle: bottom PMT only. Bottom: top PMT and bottom PMT. Red solid curve is the edge of the detector region.	32

9.11 Light collection efficiency(PDE) inside the detector region between anode grid and gate grid simulated with different PTFE reflectivity. A 90% electron collection efficiency is used.	33
9.12 Top: Mean and standard error of the distribution of the ratio between the time difference between 10% integrated area and 90% integrated area (t_{1090}) and the total drift time(t_total). Bottom: the probability of t_{1090}/t_total within the selected range.	34
9.13 The number of photons collected per electron. Blue curve is simulated assuming 1000 photons are created per electron, PTFE reflectivity=0.4, electron collection efficiency=0.9. Green curve is the closest fit with binomial profile.	35
9.14 One PMT setup light collection efficiency(PDE) inside the detector region between anode grid and gate grid. Blue: 2 mm above the gate grid. Red: in the middle between the anode grid and the gate grid. Yellow: 2 mm below the anode grid. Top: PTFE reflectivity 0.40. Bottom: PTFE reflectivity 0.75.	36
9.15 PMT areas calibration.	36
9.16 An external electron event: S1 event(first 100ns) occurred inside the scintillation region and S2 event(rest), light created by electrons passing through the scintillation region. Red line is top PMT. Blue line is bottom PMT. Black line is the sum of the top and bottom PMTs.	37
9.17 An Muon event: light created by electrons ionized by high energy muon in the scintillation region. Red line is top PMT. Blue line is bottom PMT. Black line is the sum of the top and bottom PMTs.	38
9.18 An S1 S2 event: S1 event(first 300ns) occurred outside the scintillation region and S2 event(rest), light created by electrons passing through the scintillation region. Red line is top PMT. Blue line is bottom PMT. Black line is the sum of the top and bottom PMTs.	39
9.19 A gas event: S1 event(first pulse) occurred outside the scintillation region and gas S2(else) occurred when the electrons created outside scintillation region landing on anodic grids. Top: all pulses recorded. Middle: coincidence pulses in top and bottom channels. Bottom: separate coincidence pulses. Red line is top PMT. Blue line is bottom PMT. Black line is the sum of the top and bottom PMTs.	40
9.20 Photons after a big pulse. Top: all pulses recorded. Middle: coincidence pulses in top and bottom channels. Bottom: separate coincidence pulses. Red line is top PMT. Blue line is bottom PMT. Black line is the sum of top and bottom PMTs.	41

9.21	Measured time difference between 10% integrated area and 90% integrated area ($t1090$). Solid circle: Mean and standard error. Triangle: Median and 14%, 86% percentile. Blue curve: 'coin_pulse_areas' $\in (10, 20] \text{ phe}$. Orange curve: 'coin_pulse_areas' $\in (20, 30] \text{ phe}$. Green curve: 'coin_pulse_areas' $\in (30, 40] \text{ phe}$. Red curve: 'coin_pulse_areas' $\in (40, 50] \text{ phe}$.	42
9.22	Drift velocity	43
9.23	Top: emission rate changing over time during the experiment with $v_a = +4kV$, $v_g = -4kV$. orange: area $\in (0,4]$ phe, tan: area $\in (4,30]$ phe, red: area $\in (30,1000]$ phe, pink: area $\in (1000, \infty)$ phe, green: sum of tan and red curve. Bottom: emission rate at different area changing over time.	44
A.1	An example of a detector with parallel components. The actual voltage of the i th component is V_i , the effective voltage of the i th component is $V_{0,i}$, the effective electric field on the top side of the i th component is $E_{up,i}$, the effective electric field on the bottom side of the i th component is $E_{down,i}$, etc.	64
A.2	The geometry of a single grid plane, with spacing a .	68
A.3	The geometry of a meshed grid plane, with spacing a .	69
A.4	The simulation result of grid factor for equal-spaced meshed grid.	70
A.5	The simulation result how much is the effect of the top bottom ratio of electric field on grid factor for equal-spaced meshed grid.	70
A.6	A picture of Comsol simulationsimulation.	71
A.7	The geometry of an etched grid with triangle, square or hexagon pattern.	72
A.8	The grid factor of an etched grid with triangle, square or hexagon pattern.	72
A.9	The sagging rope.	73
A.10	A membrane single grid plane.	75
A.11		76
E.1	A simple diagram of a differential pressure level sensor.	85
E.2	A simple diagram of a vertical plate level sensor and a horizontal plate level sensor.	86
E.3	A simple diagram of a parallel wire level sensor. The radius of the two wires are a . The distance between two wires is d .	87
E.4	The circuit for 2-wire RTD.	88
E.5	The circuit for 3-wire RTD.	89
E.6	The circuit for 3-wire RTD.	90
E.7	The circuit for 3-wire RTD.	90
E.8	The circuit for 4-wire RTD.	91

Chapter 1

Introduction to Time Projection Chamber.

1.1 Introduction

1.2 Time Projection Chamber

1.2.1 light, charge, heat

1.2.2 Initial state

1.2.3 S1 light

1.2.4 electron drift

1.2.5 S2 light

1.2.6 ion drift

1.2.7 heat

1.2.8

1.3 Liquid Noble Gas TPCs

1.3.1 Liquid Xenon detectors

1.3.2 Liquid Argon detectors

1.3.3 Other Gaseous Noble element detectors

1.4 Photon and electron detection

1.5 Gaseous noble gas detector

1.5.4 Energy reconstruction

1.5.5 Particle transportation

exciton, band structure, energy state level electron ion impurity neutron muon other neutral particle
electric field dependence

1.5.6 Particle energy deposition

1.5.7 Position reconstruction

1.5.8 Energy reconstruction

Chapter 2

Grid Design in detectors.

This chapter is reviewing about different grid design. This chapter is based on my simulation results and existing grid designs. field on the wire electron multiplication, photon production, electron drift and transportation, lensing, grid opacity to both photon and electron, electron energy resolution, position resolution.

2.1 Parallel Wire

2.2 woven wire

2.3 etched grid of different shape

2.4 electron emission on grid wires

2.5 secondary electron from grid wires

2.6 Material

Chapter 3

Electron emission in LUX Detector, and LZ Prototype System Test

3.1 LUX

3.2 LZ Prototype System test phase I

3.3 LZ GAS TEST

3.4 LZ

based on predictons

Chapter 4

other electron and photon sources and sink in liquid xenon detector

4.1 electron sink

Xenon ion (Xe^+) oxygen (O_2) Fluorine (F_2) Polytetrafluoroethylene (PTFE) Hydrogen ion(H^+) Hydronium (H_3O^+) Methylium (CH_3^+) Nitrogen (N_2^+) Argon (Ar^+) Krypton (Kr^+) Radon(Rn^+) alpha particle(He^{2+}) carbon dioxide (CO_2^-) nitrogen oxide nitrogen dioxide (NH^3) Hydrocarbon

4.2 electron source

Xenon(Xe) Superoxide (O_2^-) Fluorine (F_2^-) Polytetrafluoroethylene (PTFE) water (H_2O) Methane (CH_4) Nitrogen (N_2) Argon (Ar) Krypton (Kr) Radon(Rn) carbon dioxide (CO_2) Hydrocarbon

4.3 light sink

cross section of elastic scattering. Xenon exciton Xenon excited states

4.4 light source

4.5 light scattering

elastic scattering

4.6 secondary electron after S1

from LUX data.

4.7 secondary electron after S2

light induced liquid level changed induced impurity induced else random

4.8 s

ummary

Chapter 5

Electron measurement and dark matter

5.1 electron recoil background

5.2 leptonphilic model dark matter

ER

5.3 sub-GeV, small S2 dark matter

NR $j = 3e^-$

5.4 double beta decay

sensitivity dependence improvement

Chapter 6

More about gaseous noble gas detector

6.1 Introduction

6.1.1 S2

6.1.2 ionization

6.2 emission process on cathode

6.2.1 Surface field induced first emission

6.2.2 Photoelectric effect

6.2.3 ion-induced and metastable particle induced effect

6.3 breakdown in gas and liquid

6.3.1 stream breakdown

6.3.2 townsend breakdown

Chapter 7

Production and propagation of photon and electron signals in argon and xenon TPC

To view the events happening in xenon TPC, readable signals produced by the events are needed. The photon, electrons, and heat produced by an event is the most common three readable signals. And reading the primary scintillation photon signals and the secondary scintillation photon signals produced by electron luminescence via photomultiplier tubes, is one of the most common method to view the spacial and energy parameters for the events.

In this chapter, I will talk about the production and propagation of photon and electron signals in argon and xenon TPC with liquid or gas argon and xenon.

First, I will review the understanding the interactions of a common particle with the argon and xenon molecules, and the primary products of these interaction. I will discuss about the prompt light, electron and heat produced by the incident particle. And I will talk about the excitation and ionization of argon and xenon atoms and molecules.

Second, I will talk about the immediate secondary interactions of the primary products with the local argon, xenon and impurity environment. I will discuss about the recombination of argon and xenon atoms and molecules. Then I will discuss about the decay of the excitation states of argon and xenon atoms and molecules.

Then, I will talk about the transportation of the photon and electron in argon and xenon. I will talk about the elastic and inelastic scattering of argon and xenon atoms. I will talk about the reflection and absorption of the plastic and metal that we commonly used in a TPC detector. I will talk about the effect of other impurity in argon and xenon.

At the end, I will discuss about the uncertainty of the energy reconstruction from the primary

and secondary photon signals for a TPC.

7.1 Mean Free Path

7.2 Energy deposition of an event in argon and xenon

When a particle is traveling through the argon and xenon medium, it may interact with the argon and xenon atoms. These interactions transfer energy from the incident particle to the medium particles. The transferred energy could be in forms of heat, excitation, ionization, etc.

Since the electrons are much lighter than a nuclei, the average energy transfer from a collision of the incident particle for the electrons is much larger than nuclei. Using a easy case of non-relativistic kinematics, the max energy transfer in the elastic collision for a incident particle with mass m and target particle with mass M is

$$\Delta E_{max} = \frac{1}{2}mv^2 \frac{4mM}{(m+M)^2} \quad (7.1)$$

$$\approx \frac{1}{2}mv^2 \frac{4m}{M} \quad (m \ll M) \quad (7.2)$$

The energy loss of a high-energy charged incident particle in matter due to its interaction with the electrons in the medium is given by the Bethe-Bloch equation [1]:

$$\frac{dE}{dx} = \rho \frac{Z_{nucl}}{A_r} (0.307 MeV cm^2/g) \frac{Z^2}{\beta^2} \left[\frac{1}{2} \ln\left(\frac{2m_e c^2 \beta^2 \gamma^2 T_{max}}{I^2}\right) - \beta^2 - \frac{\delta(\beta)}{2} \right] \quad (7.3)$$

where,

dE/dx = energy loss of particle per unit length

Z = charge of the particle divided by the proton charge

c = velocity of light

β, γ = relative parameters $\frac{v}{c}, \sqrt{\frac{1}{1-\beta^2}}$

ρ = density of material

Z_{nucl} = atomic number of the material nuclei

A_r = relative atomic weight of the material nuclei

I = mean excitation energy in eV. It is typically around $10eV$ times Z_{nucl}

T_{max} = maximum energy transferred to electron. For all incoming particles except electrons, it is to a good approximation to $2m_e c^2 \beta^2 \gamma^2$. For electrons, it is the energy of the incident electron.

$\delta(\beta)$ = density-dependent term, for corrections at very high energy.

The equation 7.3 can be approximated to

$$\frac{dE}{dx} \approx \rho(2MeVcm^2/g) \frac{Z^2}{\beta^2} \quad (7.4)$$

Also from the incident particle energy is known, the distance of the stopping trajectory can be estimated, which is usually called the stopping range of the particle.

For the low energy charged incident particles (speed much smaller than the speed of the electrons in the material), they carry electrons along. This reduces the "effective charge" of the incident particle thus reduces the stopping power. This means sufficient corrections are required for the energy loss of heavy particles such as protons, alphas, heavy ions. Correction terms such as Barkas-Andersen-effect correction, Bloch correction, etc, which is higher order Z better illustrate the discrepancy from equation 7.3 are also considered for computer programs for calculating stopping power and range tables for electrons, protons, and alpha particles, such as ESTAR, PSTAR, ASTAR [2]. Also for even more high energy incident particles ($> 10MeV$), radiative stopping such as bremsstrahlung radiation, cherenkov radiation and pair production is predominant.

The result of stopping power for the most common argon and xenon isotope 40Ar and ${}^{129}Xe$, ${}^{131}Xe$, ${}^{132}Xe$ is shown in figure ??, ???. Xenon has density of $2.8608g/cm^3$ and $0.017960g/cm^3$ at saturation liquid and gas at 177 K, ???. The stopping range for an electron of energy $200keV$ is $\sim 0.028cm$ and $4.46cm$. The stopping range for an alpha particle of energy $2MeV$ is $\sim 0.0014cm$ and $0.225cm$

The distribution of the process for an electron falling on a cylindrical wire can be written estimated to a Polya distribution, ??

$$P(N) = \frac{1}{\mu} \frac{(\theta + 1)(\theta + 1)}{\Gamma(\theta + 1)} \left(\frac{N}{\mu}\right)^{\theta} \exp(-(\theta + 1)\frac{N}{\mu}) \quad (7.5)$$

where, μ is the mean of electron gain around the wire.

Polya distribution is a reparameterization of Gamma(Γ) distribution, which has probability distribution function

$$P(x) = \frac{\beta^\alpha}{\Gamma(\alpha)} x^{\alpha - 1} \exp(-\beta x) \quad (7.6)$$

with shape parameter α , and rate β

$$\mu = \frac{\alpha}{\beta} \quad \theta = \alpha - 1 \quad \alpha = \theta + 1 \quad \beta = \frac{\theta + 1}{\mu} \quad (7.7)$$

Chapter 8

Metal in detector

8.1 Metal in Vacuum

8.1.1 I-V curves

8.1.2 Fowler-Nordheim Plot and Surface factor

8.1.3 Shortkey Barier and

8.2 Metal in Liquid

8.2.1 Band Structure

In [3], liquid xenon band structure, In [4], solid xenon band structure.

8.2.2 Liquid "Work Function"

8.2.3

8.3 Treatment of Stainless to reduce emission

8.3.1 polishing, passivation, gas conditioning

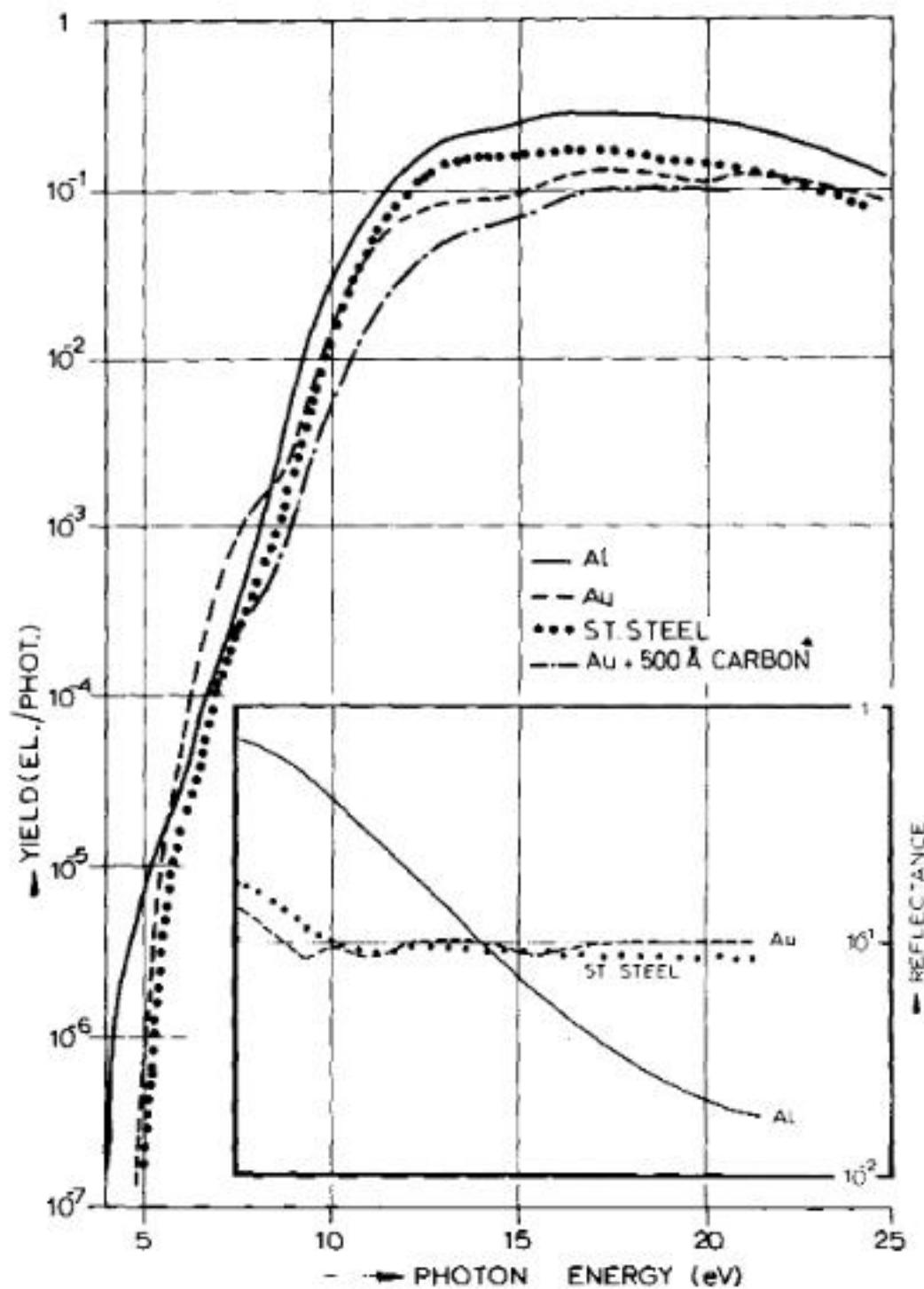


FIG. 1. Photoelectric yield per incoming photon for Al, Au, stainless steel, and for gold overcoated with 500 Å of carbon. The reflectance at near-normal incidence for Al, Au, and stainless steel is shown on the inset.

Chapter 9

Gas phase xenon detector for wire testing

For understanding the grid electron emission in LZ detector, we designed a gaseous xenon detector to test the grid behavior in a similar environment as the LZ detector. It's very interesting to see the emission events from the grid in different operating voltages. It would help us figure out the optimized operation voltages for our detector and study different method for reducing the electron emission background. Reducing of the electron emission from the grid wires will significantly improve our sensitivity to low energy events and our understanding of low mass WIMPs. It would also help to keep the trigger environment quieter, so that the quality of the S1 and S2 signals that we rely on for events classification and energy reconstruction contains less systematic errors.

The detector we build, in the latter context "Gas Detector", is consist with two major parts: the operation system and data acquisition system.

The operation system contains four parts: the tested grids, the gas handling and distribution system, the high voltage system and the light collection system. The gas handling and distribution system is for delivering and storing quality pure gas to the Gas Detector. It includes the operation chamber, the gas circulation panel and plumbing, pressure and temperature sensors of different range, and a separated purity measurement system. The high voltage system includes the power supply, high voltage feed through, cables, and cable termination. The light collection system for measuring the quantity of scintillation light created in the detector includes two PMTs, and the PTFE light reflector.

The data acquisition(DAQ) system is attached directly onto the output of the two PMTs. It does PMT pulse amplification, shaping, digitizing, transferring and storing.

The recorded events were passed to a data processing framework to reduce the dimensions of the input data. Then, the reduced quantity data(RQs) were sent for event classification to select the

interesting events. Because of the rate of the electron emission event we are mostly interested in has a various range, in some case really rare. A studying of background events for its the pulse shape, and energy distribution were done to reduce the uncertainty of the emission event rates. And this also helps to give a electron emission selection efficiency.

Simultaneously, a light creation and propagation simulation were done for different event classes at different locations to confirm the pulse shape for different event classes.

Finally, the knowledge of event classification were used to study the electron emission from different tested grids that we measured.

In this chapter, I will first introduce the design concepts of each individual components in detail about Gas Detector that we designed for measuring the electron emissions. Then I will talk about the data processing framework. Then, I will talk about the light creation and propagation simulations in the detector for the electron emission events. I will discuss about characteristic pulse shape and rate of the background events, along with the simulations for these events. Finally, I will discuss about the results from different grids from this detector.

9.1 The gas phase xenon detector

The gas phase xenon detector, in the latter context "Gas Detector", is designed for testing 1% scale LZ grids, which are also tested in LZ system prototype phase I detector(Phase I Detector). The Gas Detector has one chamber, a gas circulation panel, an digitizing readout system.

9.1.1 The Chamber

he detector we build is with argon and xenon gas from pressure between $10^{-5}bara$ to $3.5bara$

9.1.2 Test Mass

There are photomultiplier tubes(PMT)

9.1.3 DAQ system.

9.1.4 External trigger

9.1.5 High voltage feed through and inside outside cable connectors

9.1.6 Gas circulation system

Fig: 9.6 shows the gas circulation panel. This panel is designed to also continuing purification of noble gas element in the detector so that the same gas purity condition. A PS3-MT3-R-1 SAES rare

	Top PMT	Bottom PMT
Serial Number	KB1163	KB1170
Cathode Luminous Sens. ($\mu A/lm$)	149.0	148.0
Anode Luminous Sens. (A/lm)	657.0	1010.0
Anode Dark Current (nA)	1.00	4.60
Cathode Blue Sens. Index	12.60	12.30
Q.E. (%)		
165 (nm)	22.1	21.2
170 (nm)	33.3	32.6
175 (nm)	36.3	36.0
182 (nm)	37.1	37.0
188 (nm)	36.1	36.2
194 (nm)	33.9	34.1
200 (nm)	32.6	32.9

Table 9.1: Spectral response of the PMTs tested in HAMAMATSU

gas purifier getter is using heated ? to purify the rare gas in the detector. The getter element has a sub-ppb efficiency of removing water, nitrogen, oxygen, carbon oxide, carbon dioxide, hydrogen and hydrocarbons. And the capacity of the getter is *howmany* in volume of nitrogen and oxygen. With continue purification, noble xenon gas achieves a purity of better than *howmany*. A custom KNF pump is used to drive the gas circulation in the system. The pump is a model *modelnumber* double diaphragm pump, which has company specified *2bara* operation pressure. During the real operation, the pump is working at pressure less than *3.7bar*. The diaphragm pump shows leak rate less than $10^{-7}bara * l/s$. The circulation flow rate is controlled by a *modelnumber* mass flow controller, that has maximum flow rate at *5slpm*.

9.2 Sparking in the system

Before safely turning on the PMTs to measure the light emission from the grids, a series of sparking test were done to figure out the high voltage behavior and high voltage weak points in the system. Improvements were done to attempt to eliminate the light emissions from spots other than the grids. And the maximum voltage that the grids can hold are measured with different gas and different pressures.

9.2.1 The sparking on the high voltage feed through connectors

9.2.2 The sparking on the cable grounding terminations

9.2.3 The sparking between the grids

9.3 Light propagation Simulations

9.3.1 Light creation

(original text) There are three kind of light creation resources in the detector that is able to be collected by the PMT readout system: 1) dark current from PMT photo cathode and diodes, 2) background light from the material of the detector and outside detector region, 3) scintillation xenon light coming from an event happened in the detector region. Among these, the third one includes the electron emission events that we want to study. The first light resource is mostly thermionic emission from the PMT photo cathode material, which normally has low work function to achieve high photo electron conversion efficiency for the PMT tube. Because of each thermionic emission is independent event, dark current normally comes in forms of single electrons. So even though these type of light is dominant. However, a series of dark current event may look like a real event and contribute to false classifying event rate(false coincidence event). The second light resource has varies origins. During the sparking test, we observe visible light along with discharge coming from the high voltage feed through connectors, high voltage cable termination connectors, and high voltage cables, etc. These discharge current originated from the imperfect points on the metal surface generate xenon scintillation light outside the detector region. This current grows exponentially(following Fowler Nordheim field emission equation) with the electric field on the metal surface. However, the light collection efficiency on the outside detector region is low. Thus, an event with several photons from outside detector region also looks like a electron emission event. But, the event of electron emission from the grids have a more specified time span from the drift time of the electron between the two grid planes. We can distinguish these two type of events from these features. This feature can be use for distinguishing this background. Fluorescence light from the PTFE surface were also observed. Fig: 9.7, shows the decaying of PTFE fluorescence. To reduce this background, sparking is avoiding for emission studying. Three-day waiting time for quieting the detector was taken before each measurement.

(dan's version of above paragraph is split into three short paragraphs) The primary source of light that we are interested in is electroluminescence from electrons emitted from a grid into the active region. Using pulse timing characteristics, we are able to distinguish this source from two classes of unwanted backgrounds that are also visible in the PMTs. Pulses from active-region electron-emission events are characterized by a unique width in time. The electroluminescence is produced in the fixed gap between the grid planes during the transit of the electron and the drift velocity is determined

by the electric field strength in that gap.

The first unwanted class is produced by electrons outside the active region and has a variety of origins. During a sparking test we observed visible light through a glass viewport from discharges coming from the high-voltage feed-through connectors, the high-voltage cable termination connectors, and the high-voltage cables. These discharges originate from imperfections on the metal surfaces and exhibit currents that grows exponentially with electric field, consistent with the Fowler-Nordheim field emission equation. Even though these are relatively strong sources of electrons, the pulse heights are comparable to active-region events because the light collection for external events is poor. However, since the electrons from these sources are emitted from outside the detector region, they have a wide-ranging time structure since the gaps and fields are not well defined, allowing them to be distinguished from active region events.

The second class of unwanted events are due to dark current from the PMT photo cathode and dynodes. This process originated from thermionic emission from the PMT photo cathode material, which by design has a low work function to achieve high photoelectron conversion efficiency. Because each thermionic emission is uncorrelated, this dark current typically appears as isolated single electrons. Even though these events dominate the rate, they only occasional produce random coincidences that mimic active-region events. (end of Dan's edits)

Fluorescence light from the PTFE surface were also observed. Fig: 9.7, shows the decaying of PTFE fluorescence. To reduce this background, sparking is avoiding for emission studying. Three-day waiting time for quieting the detector was taken before each measurement.

The third type of light resource, xenon scintillation light, is



Penning effect



9.3.2 Light collection efficiency

The light collection efficiency

9.4 DAQ configuration, DAQ dead time and Required silence pre-trigger

9.5 Data processing

9.6 PMT single photo electron area calibration

	Top PMT	Bottom PMT
Single phe area ($mV \cdot ns$)	437 ± 148	643 ± 162

Table 9.2: PMT areas calibration.

9.7 Understanding of the events

For clearly studying the grid wire electron emission events in the detector, understanding different types of background event rates events is necessary. To study this, first understanding the resources of these background and the general pulse shape of these events is necessary.

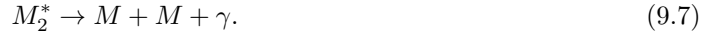
In this section, I will discuss about they different type of event happening in the detector. I will mainly focusing on discussing on the shape and the rate of these events and their impedance from these type of background events on the electron emission study.

The event class that we want to study are:

- Electron emission events from the grid wires.
- Electron emission events from the grid holding plates.

Electron emission events from the grid wires can be studied by the electroluminescence light from the emitted electrons. After the emitted electrons left the cathodic metallic grid, they would drift to the anodic grid by the Comlomb force between the two grids. During this process, these electrons will gain energy and accelerate from the Comlomb potential. The high speed electrons will lose their energy and create secondary particles through three processed. 1)exciting the gas atoms/molecules

on their path, 2) ionizing the gas atoms/molecules on their path, or 3) or elastic scattering with the gas atoms/molecules on their path. The excited gas atoms/molecules would de-excite after a short amount of time and emit scintillation light photons. Usually these scintillation light photons were able to be re-absorbed by the gas atoms/molecules because they have a similar energy compare to the exciting states of the gas atoms/molecules. However, for noble gas molecules, another type of deexcitation would happen. The excited noble gas molecule would find another noble gas molecule and found a two noble gas atom molecule excitation state. The two atom molecule, sometimes called a dimer, could also deexcite and emit a photon.



However, this photon would have a different energy compare to the excited state of noble gas atom. Thus, this photon would propagated a further distance. The number of scintillation photons are mostly depending on the total Comlomb potential the electron gains from the trajectory and the energy loss by thermal inelastic scatterings. The former is a function of the potential difference between the two grids, when the latter is mostly a function of the length of the electron trajectory. The secondary scintillation light is found to have a linear dependence on the reduced field E_s/N [6], where E_s is the field strength in the scintillation light creation region and N is the density of gas:

$$\frac{dL_s}{dx} = a \frac{E_s}{N} + b \quad (9.8)$$

$$\cdot \quad (9.9)$$

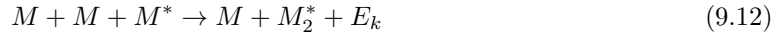
The parameters a and b were found to be

$$a = 0.137(2) \frac{ph}{e \cdot V}, \quad (9.10)$$

$$b = -4.7(1) \times 10^{-18} \frac{ph}{e} \frac{cm^2}{atom}. \quad (9.11)$$

Thus, with counting the scintillation photons over time, a grid emission event can be distinguished from the other type of events that occurred in the detector, which would be discussed late in this paragraph.

The excited dimer molecules can be separated to two types, the singlet state and triplet state. The singlet state, written as ${}^1\sigma_u^+$, ${}^3\sigma_u^+$, the triplet state, written as ${}^3\sigma_u^+$, ${}^1\pi_u^+$, are known to be created from a three-body deconstruction of noble gas atom excited state ${}^2P_{1/2}$ state and ${}^2P_{3/2}$ state.



(9.13)

Because the creation process is a three body reaction, the creation rate of the these two states have strong dependence on the gas density of atoms. The decay time of both of these two states have a dependence on the gas density. [7]. Some other materials also show that the decay time is very different between liquid noble gas and very dense noble gas.

The decay time for the singlet state and the triplet state in liquid xenon are $4.3 \pm 0.6\text{ns}$ and $22.0 \pm 2.0\text{ns}$ [8]. And for dense xenon, 2.7 to 32atm, the decay time for singlet states varies from $15 \pm 3\text{ns}$ to $5.5 \pm 1\text{ns}$. The decay time for triplet state is $96 \pm 5\text{ns}$ in the same pressure range.

The decay time for the singlet state and the triplet state in liquid argon are $7.0 \pm 1.0\text{ns}$ and $1.6 \pm 0.1\mu\text{s}$. And for dense argon, the decay time for singlet states is $4.20 \pm 0.13\text{ns}$. The decay time for triplet state is $3.2 \pm 0.3\mu\text{s}$

The ionization of gas atoms/molecules happens along with scintillation process. When the incident electron exceed the ionization energy of the gas atoms/molecules, their is a chance that an inner shell electron would leave the gas atoms/molecules. The cross-section of ionization are excitation probabilities as a function of incidence electron are shown in ???. The ionization probability increase as the energy of incident electron. In a higher electric field space or a lower gas density situation, the average energy an electron can gain between each collision is higher. Thus, ionization are more commonly seen in these situation.

A critical threshold electric field density is where ionization become important ($\gtrsim 1\%$) for gas. During our operation, the electric field between the two grids are much smaller than this critical threshold, while the electric field on the surface of the grid is sometimes higher than this critical threshold. Very few ionization events happens in the main scintillation region, and most of the ionization happens around the grid wires. This is consistent with what we saw in data.

The creation of excitation photons and ionization atoms and secondary electrons are also studied with simulation software. The

The backgrounds in the detector can be separated to three categories: noise, external and internal particle events and others. These background events are:

- Electronic noise Electronic noise is the irreducible

Electronic noise type 1: photomultiplier tube(PMT) noise Photomultiplier tube noise is coming from the thermeonic emission

Electronic noise type 2: building power supply noise

- External and internal particles

- Radiation from the detector component

- High energy muon from cosmic rays

- High energy external gamma

- Other trouble:

- photomultiplier tube(PMT) baseline shifting

- photomultiplier after pulsing

- two photo electron accidental false coincidence in two photomultiplier tubes(PMT)(dark current)

- discharging from the cable feed through and connectors.

- delayed light from big events (Polytetrafluoroethylene(PTFE) fluorescence)

External and internal particles in the gaseous medium will deposit their energy on their trajectory.

- S1 light: initial scintillation light from direct scintillation of gas molecules and immediate recombination of ionized gas molecules and electrons

- S1 inside the scintillation region (between the two grids)

- S1 outside the scintillation region , the anodic biased grid side

- S1 outside the scintillation region , the cathode biased grid side

- Gas S2 light: scintillation light created from electrons outside scintillation region landing on the anodic bias grid

- S2 light: scintillation light created from electrons passing the scintillation region

S1 event:

9.8 Drift velocity calibration

9.9 Electron emission changing over time

During the experiment, an increasing of electron emission over time was observed. And the reason of this phenomenon is possibly the rearranging of the electric field in the detector around the grid wires. Because of the difference between the drift velocity of the electrons and the ions. Electrons moves faster thus vanish earlier comparing to ions. This results in a positive charge environment in the detector especially around the grid wires that is being studied. The increasing of the density of ions would enhance the electric field around the grid wires, thus increase the electron emission from them. For clearly studying this problem, a series of dataset were taken every 10 minutes with operating the anode and the gate grid steadily at $+4, -4\text{kV}$. Fig: 9.23 shows the rate changing over time during the experiment. Studies shows that the emission enhancement was stronger at coincidence pulse area smaller than 30 phe and was very weak at larger coincidence pulse area. This indicates that the excess events seen may come from the enhancement of single electron emission and the light accompany with it.

9.10 The influence of impurity in xenon

9.11 The influence of long operation duration

9.12 The influence of grid passivations

9.13 Discussion about LZ grids

Grid Name	Top PMT	Anode	Gate	Cath	Bottom	Bot PMT
Location from liquid surface (mm)	78	8	-5	-1461	-1598.5	-1608.5
Operation Voltage(kV)	-1.5	5.75	-5.75	-50	-1.5	-1.5
Wire Pitch (mm)	NA	2.5	5	5	5	NA
Wire Diameter (um)	NA	100	75	100	75	NA
Tension (N)	NA	2.5	2.5	2.5	2.5	NA
Deflection (mm)	NA	0.59	0.61	0.19	0.19	NA
Wire Surface (m^2)	1.665	0.423	0.159	0.212	0.158	1.665
Average Surface Field (kV/cm)	1.0	43.7	-51.0	-30.1	33.1	0.4
Wire Top max Surface Field (kV/cm)	NA	39.2	-53.7	-28.5	35	0.3
Wire Bot max Surface Field (kV/cm)	1.0	-48.2	48.3	31.6	-31.2	NA

LZ grids parameters

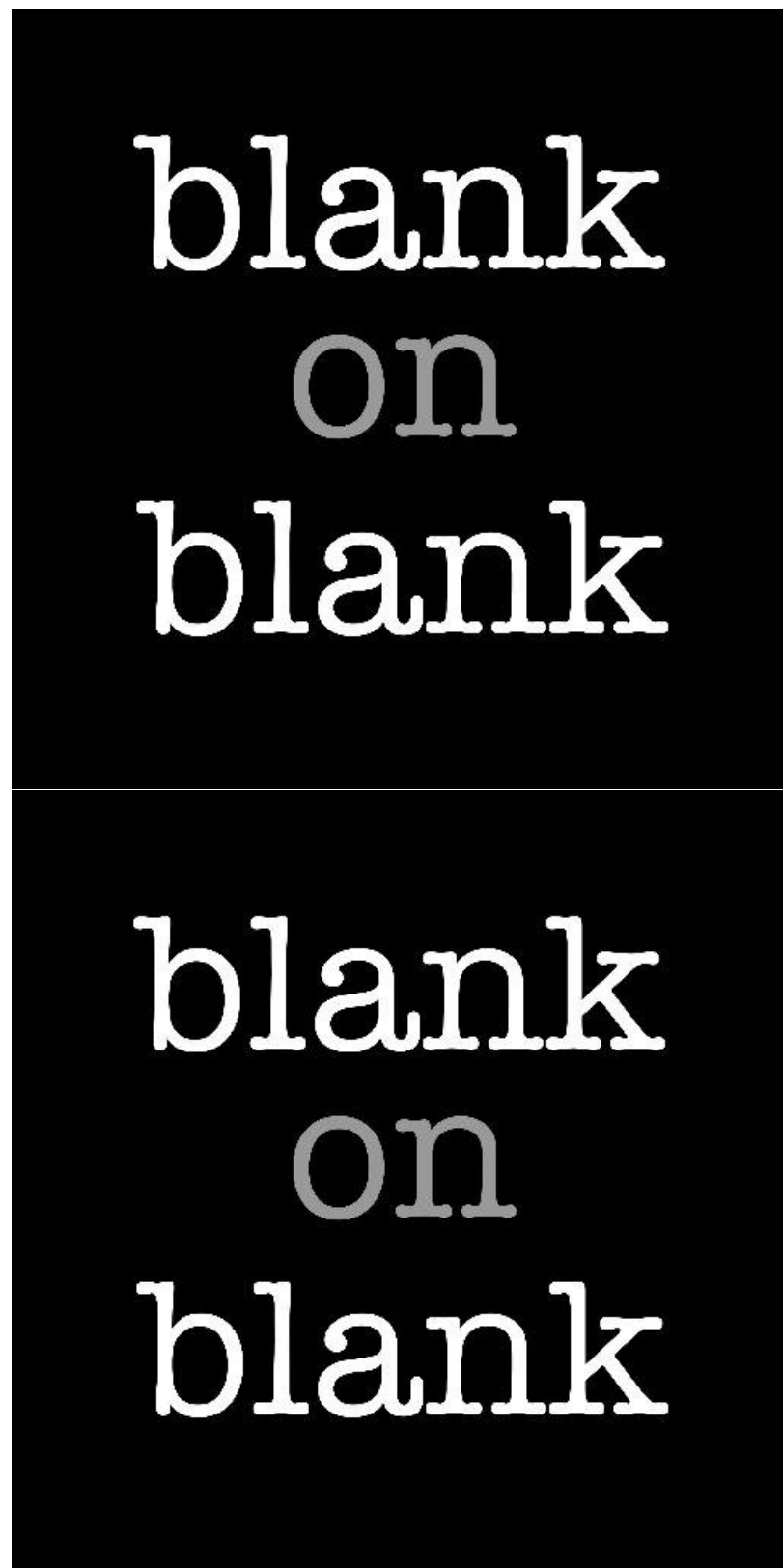


Figure 9.1: Top: The Gas Detector without the outer vessel. Bottom: The Gas Detector with the outer vessel assembled. On top of the deck is the electronic and gas gauge breakouts. On the right is the vacuum pumping system.



Figure 9.2: Left: one PMT setup. Right: two PMT setup.

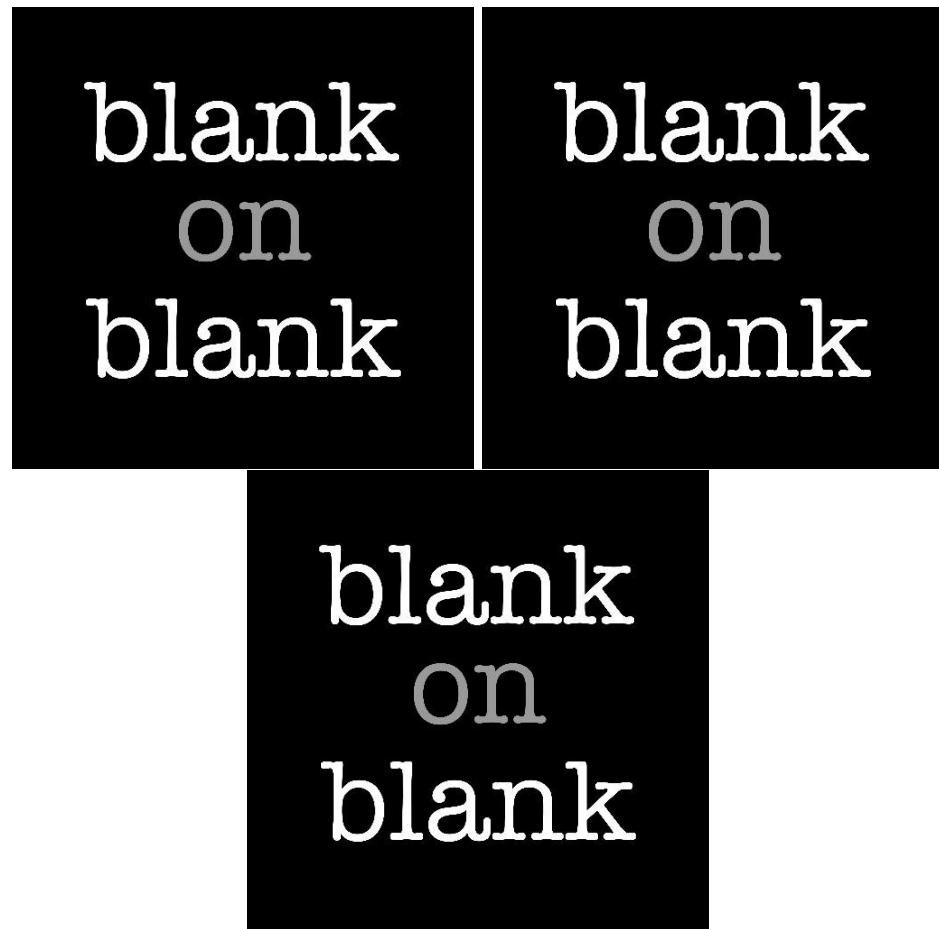


Figure 9.3: Top left: the amplifier. Bottom left: the digitizer. Right: the back side of the Gas Detector.

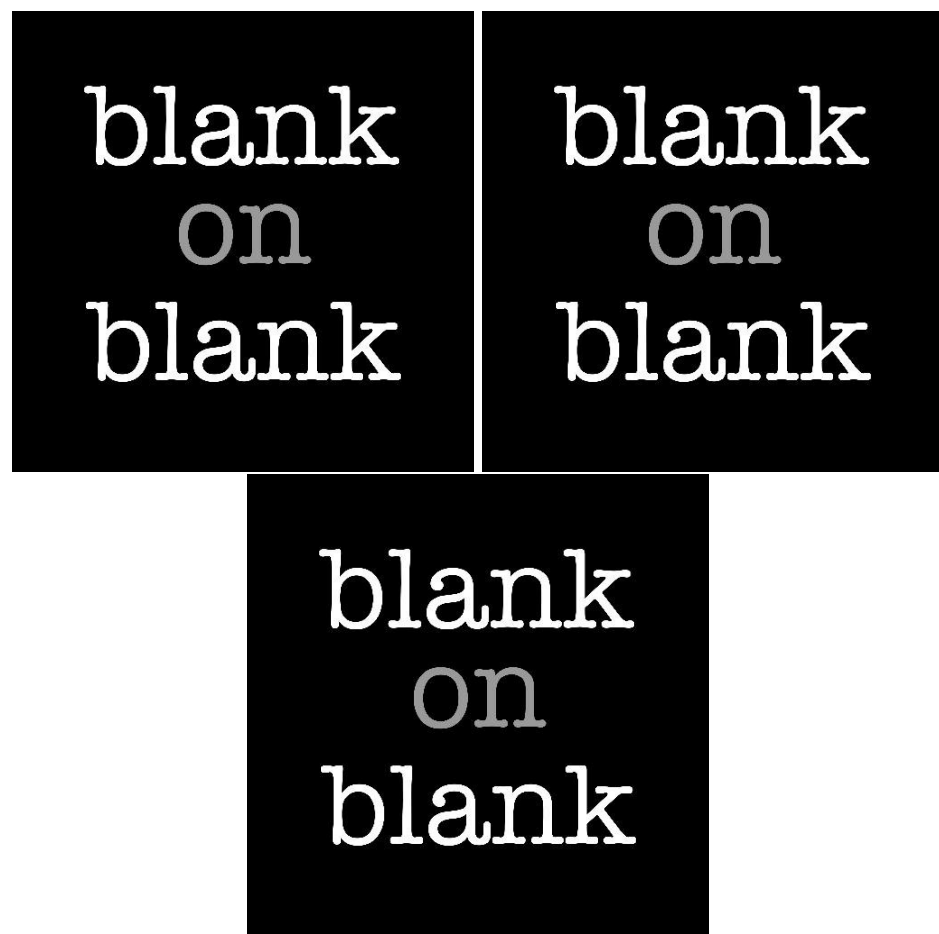


Figure 9.4: External trigger system

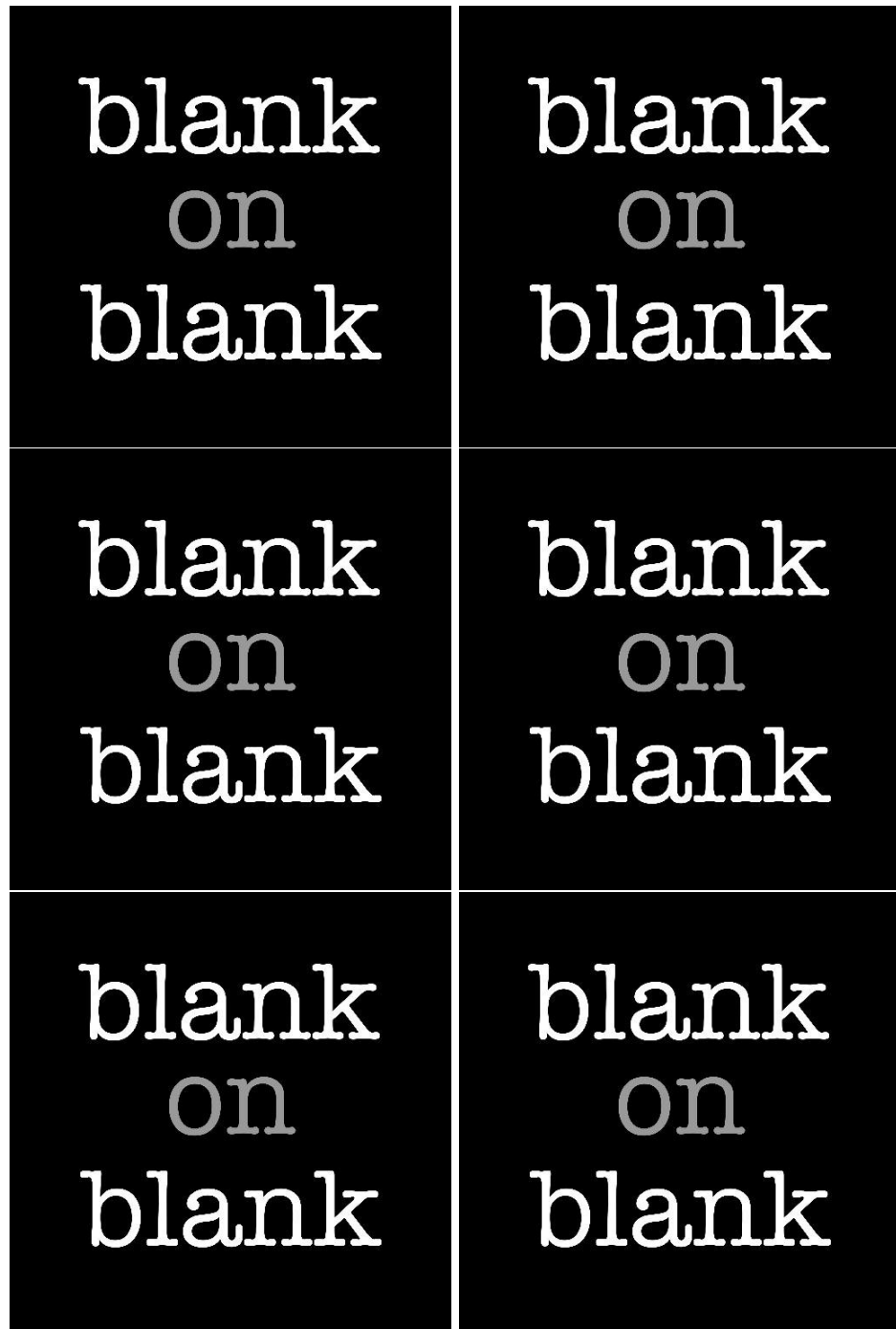


Figure 9.5: Top: ceramic feed through. Middle: external filter boxes. Bottom: internal cables and connectors.

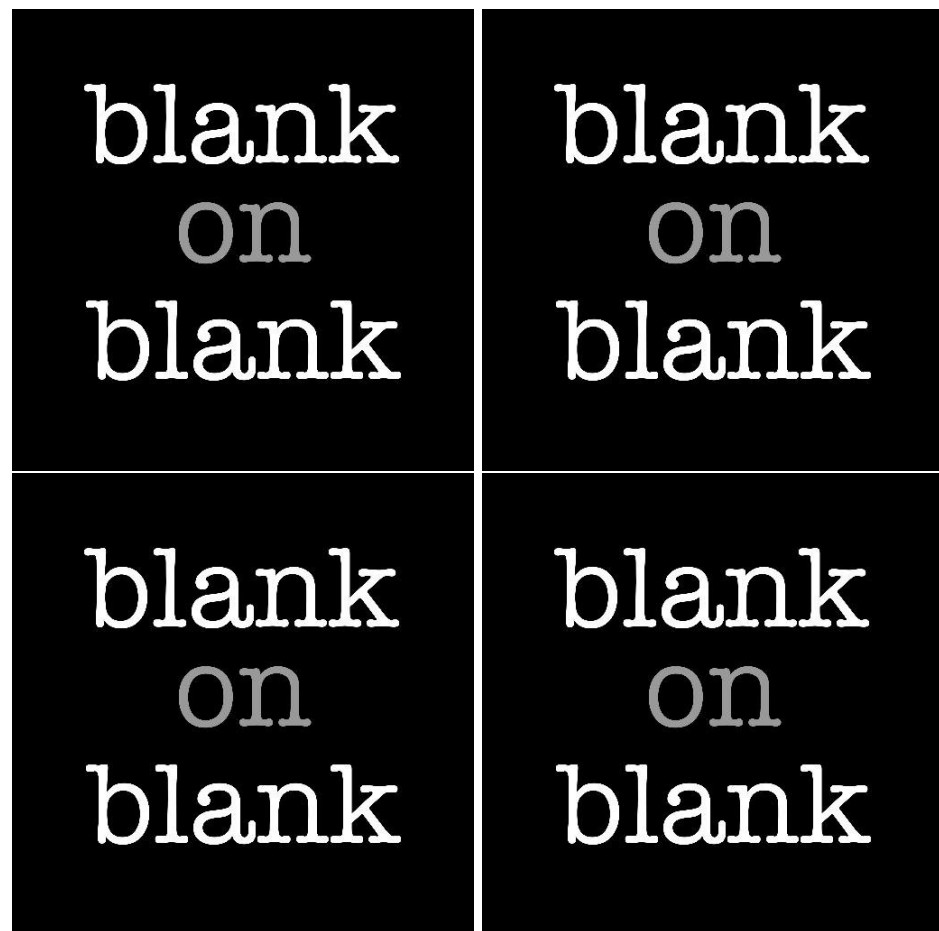


Figure 9.6: Top left: KNF circulation pump. Middle left: storage bottles. Top right: the gas circulation panel. Bottom: the gas circulation panel Piping and Instrumentation Diagram (P&ID)



Figure 9.7: Fluorescence light from the PTFE surface decaying with time

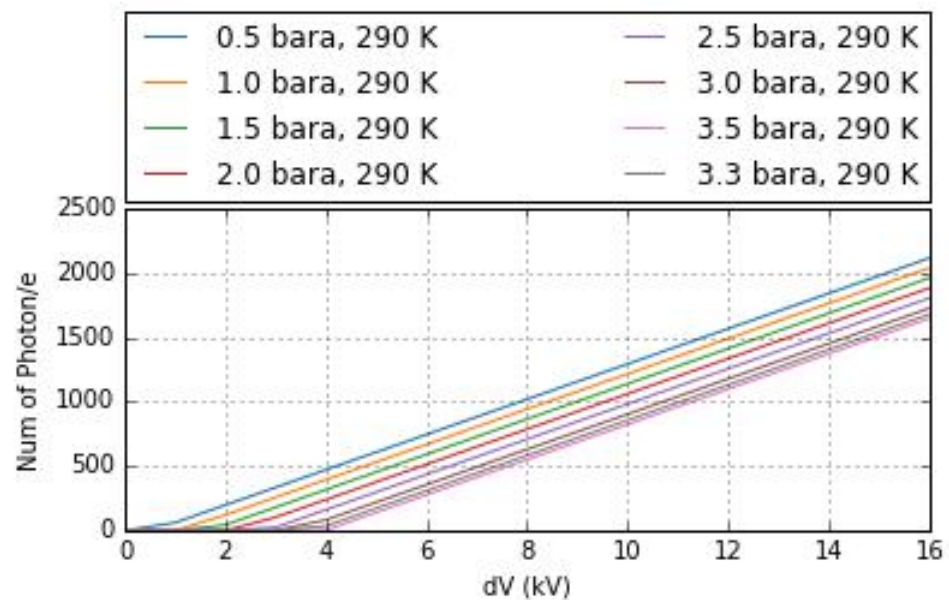


Figure 9.8: The number of photons created per electron between the anode grid and the gate grid. A 13mm gap size is assumed.

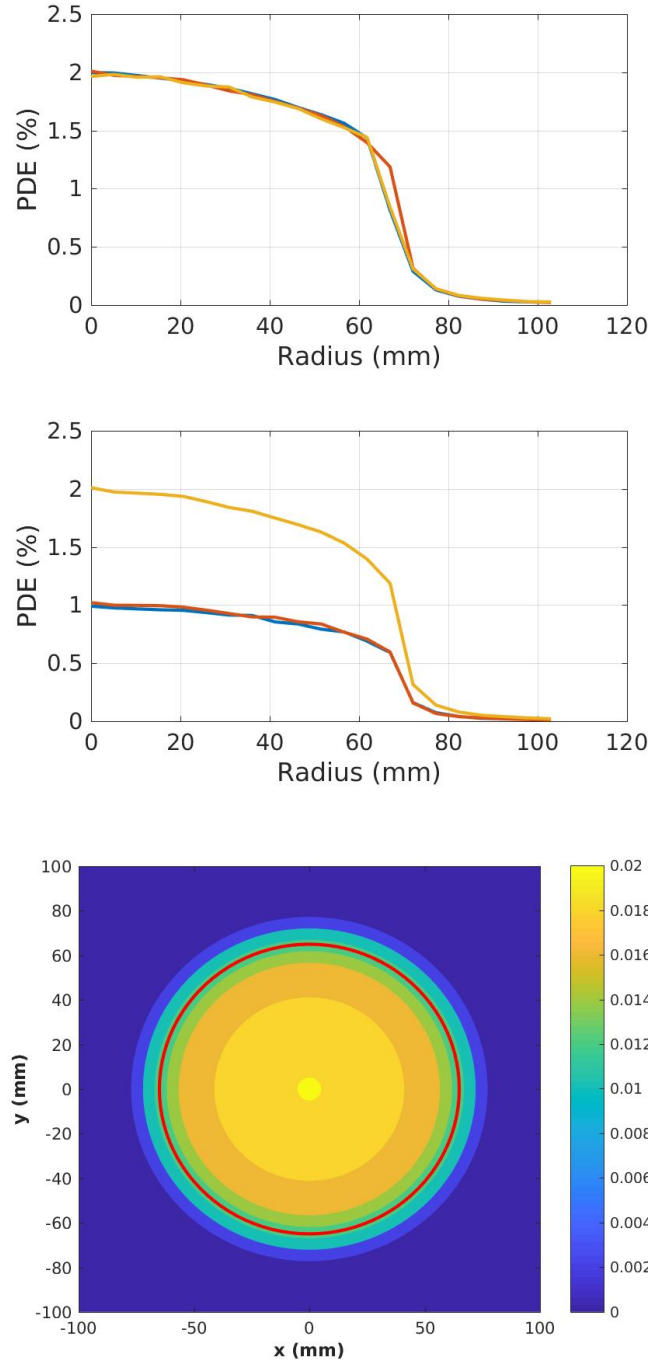


Figure 9.9: Light collection efficiency(PDE) inside the detector region between anode grid and gate grid(simulated with PTFE reflectivity of 0.40). Top: light collection efficiency vs radius from the center of the grid ring at different location. Blue: 2 mm above the gate grid. Red: in the middle between the anode grid and the gate grid. Yellow: 2 mm below the anode grid. Middle: top and bottom PMT light collection efficiency. Blue: top PMT. Red: bottom PMT. Yellow: total. Bottom: light collection efficiency in the middle between the anode grid and the gate grid. Red solid curve is the region of the grid wires.

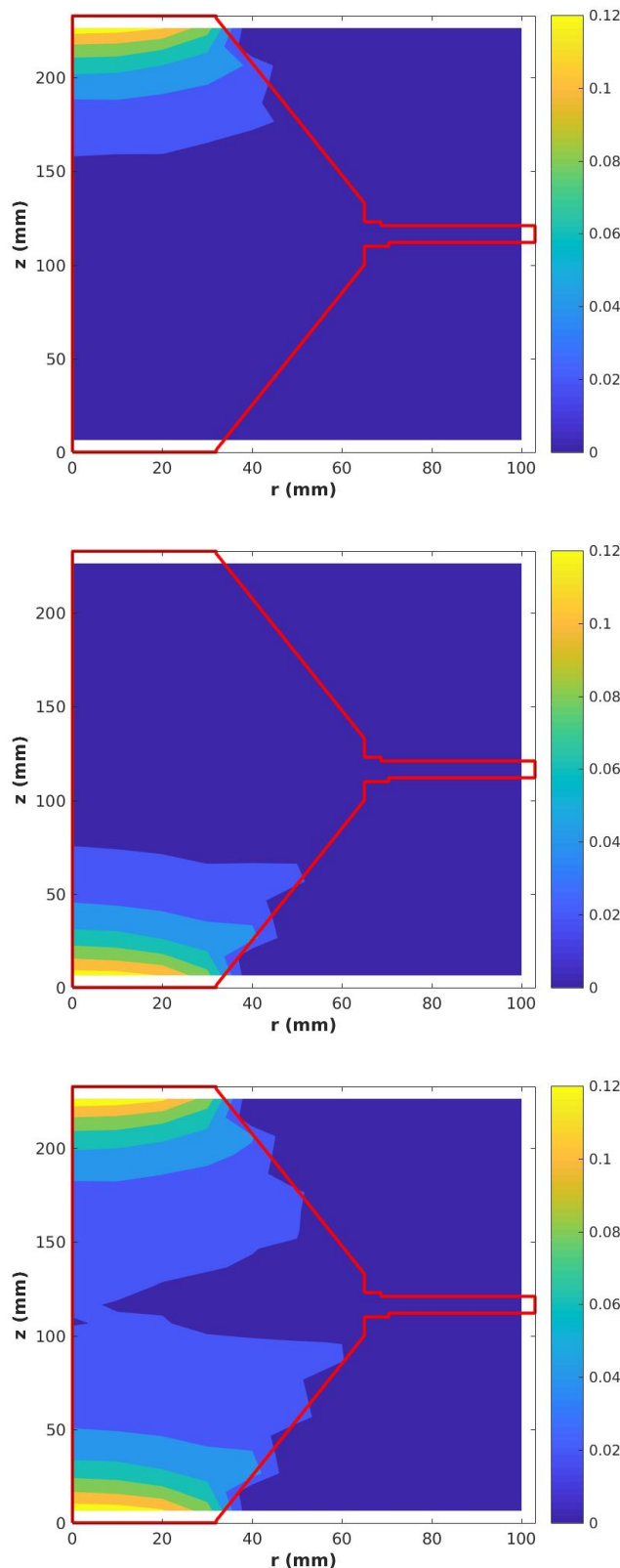


Figure 9.10: Light collection efficiency inside the detector region rz cross section (simulated with PTFE reflectivity of 0.40). Top: top PMT only. Middle: bottom PMT only. Bottom: top PMT and bottom PMT. Red solid curve is the edge of the detector region.

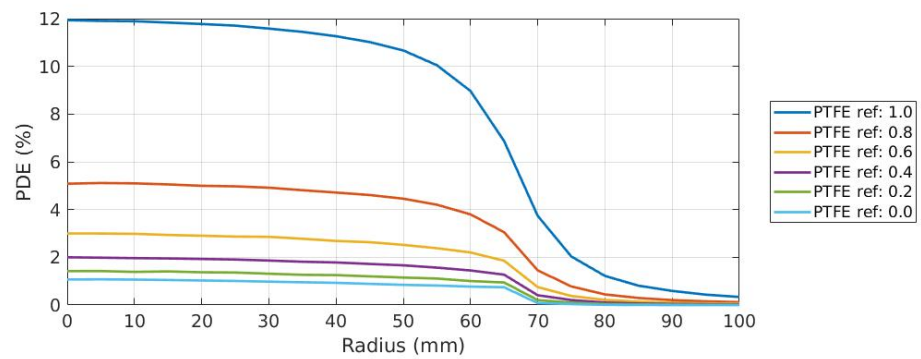


Figure 9.11: Light collection efficiency(PDE) inside the detector region between anode grid and gate grid simulated with different PTFE reflectivity. A 90% electron collection efficiency is used.

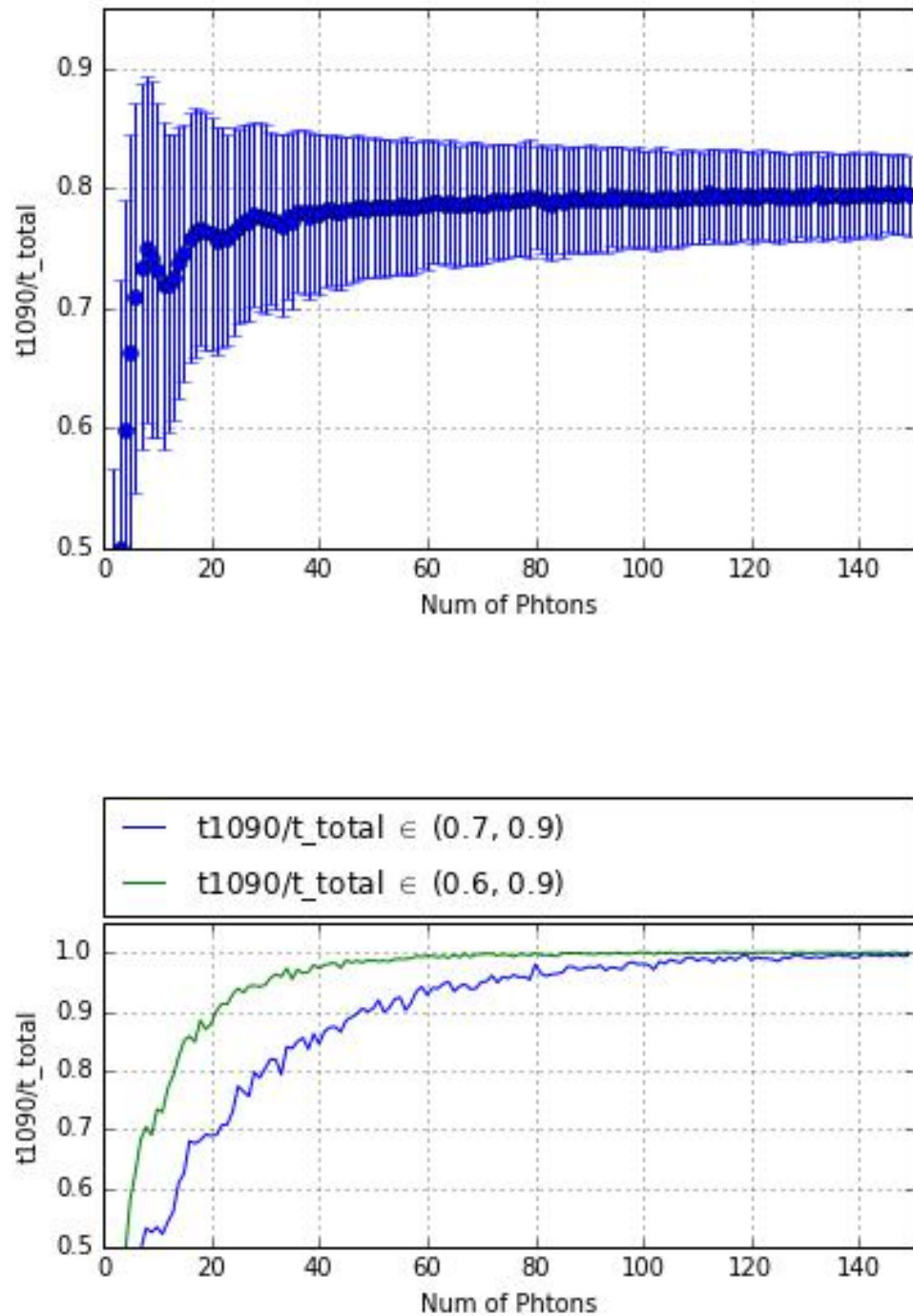


Figure 9.12: Top: Mean and standard error of the distribution of the ratio between the time difference between 10% integrated area and 90% integrated area (t_{1090}) and the total drift time(t_{total}). Bottom: the probability of t_{1090}/t_{total} within the selected range.

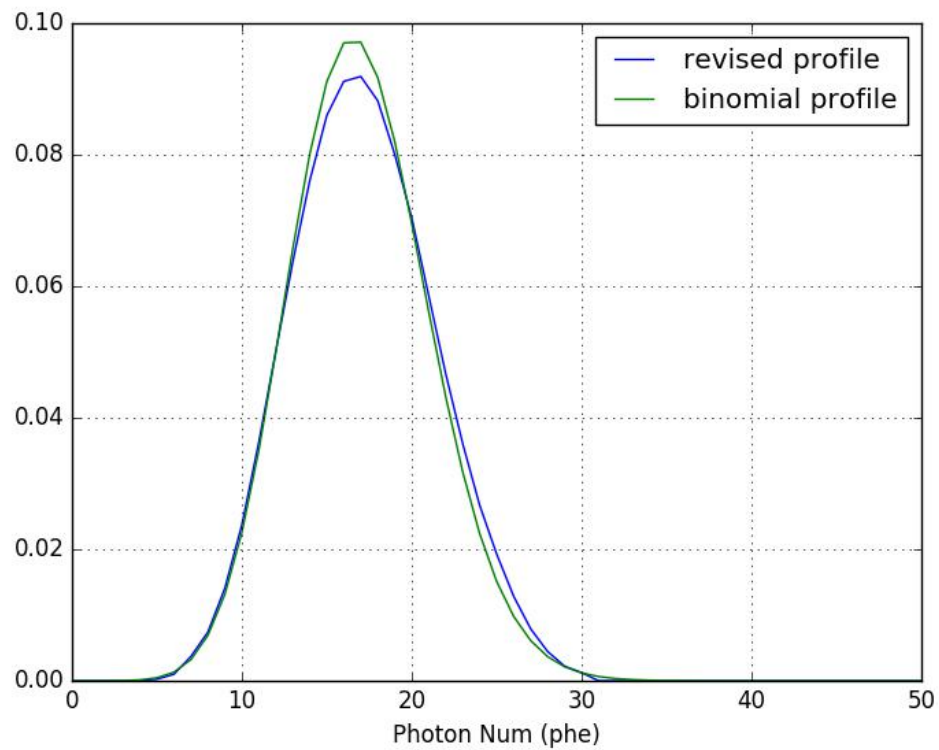


Figure 9.13: The number of photons collected per electron. Blue curve is simulated assuming 1000 photons are created per electron, PTFE reflectivity=0.4, electron collection efficiency=0.9. Green curve is the closest fit with binomial profile.

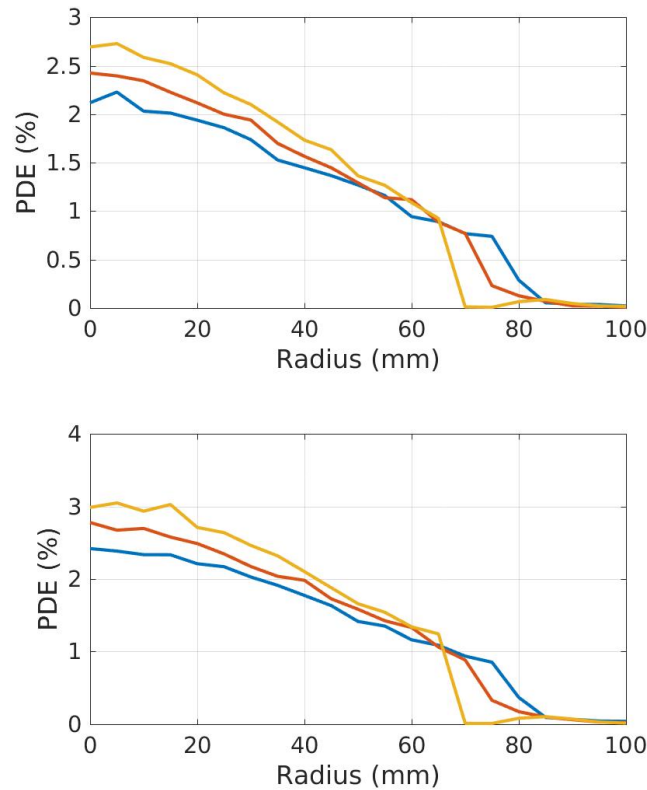


Figure 9.14: One PMT setup light collection efficiency(PDE) inside the detector region between anode grid and gate grid. Blue: 2 mm above the gate grid. Red: in the middle between the anode grid and the gate grid. Yellow: 2 mm below the anode grid. Top: PTFE reflectivity 0.40. Bottom: PTFE reflectivity 0.75.

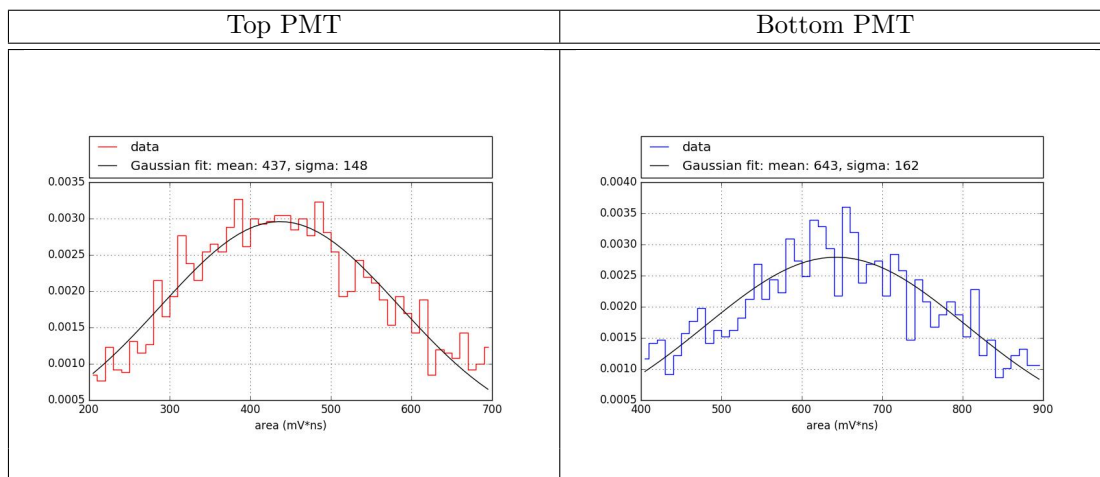


Figure 9.15: PMT areas calibration.

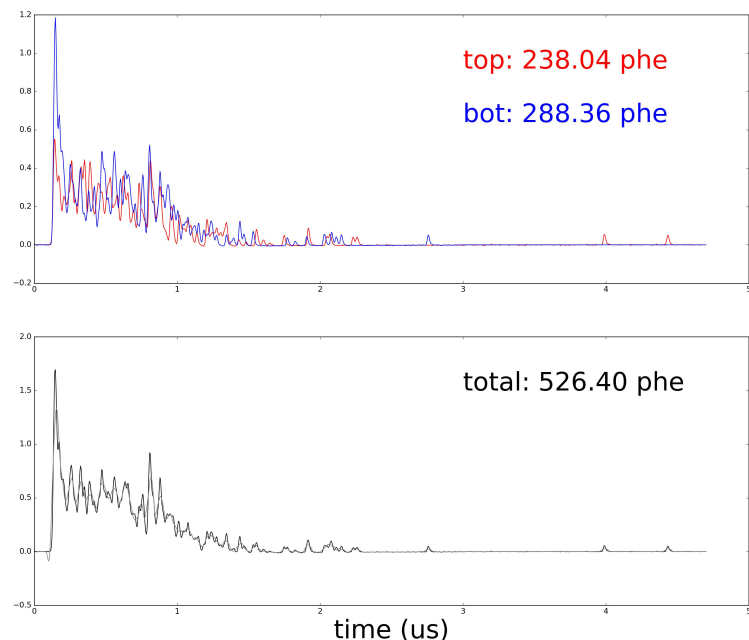


Figure 9.16: An external electron event: S1 event(first 100ns) occurred inside the scintillation region and S2 event(rest), light created by electrons passing through the scintillation region. Red line is top PMT. Blue line is bottom PMT. Black line is the sum of the top and bottom PMTs.

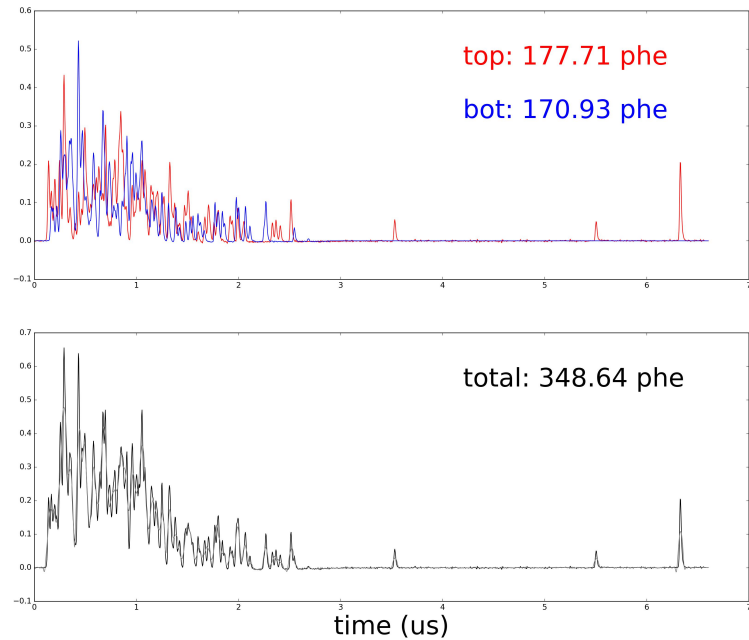


Figure 9.17: An Muon event: light created by electrons ionized by high energy muon in the scintillation region. Red line is top PMT. Blue line is bottom PMT. Black line is the sum of the top and bottom PMTs.

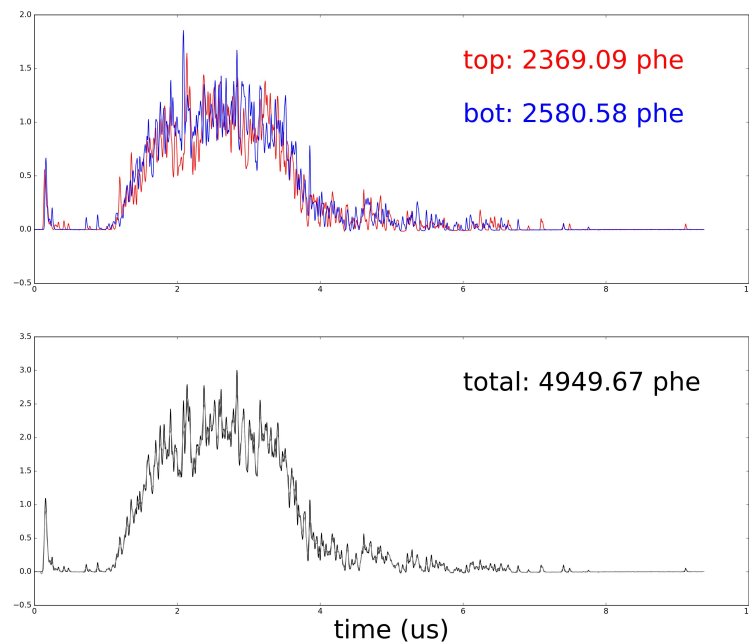
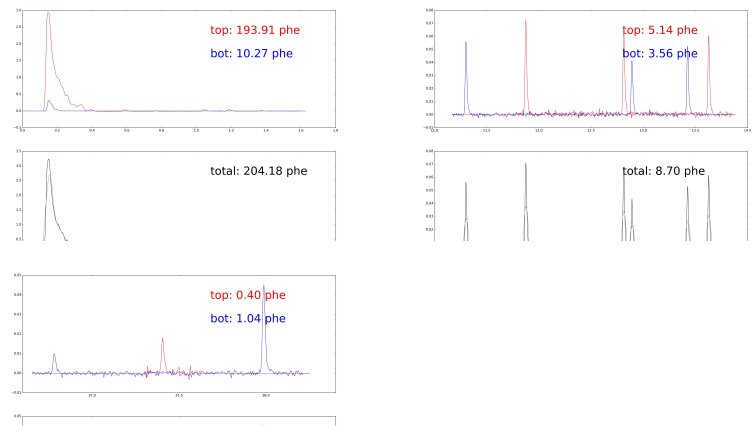
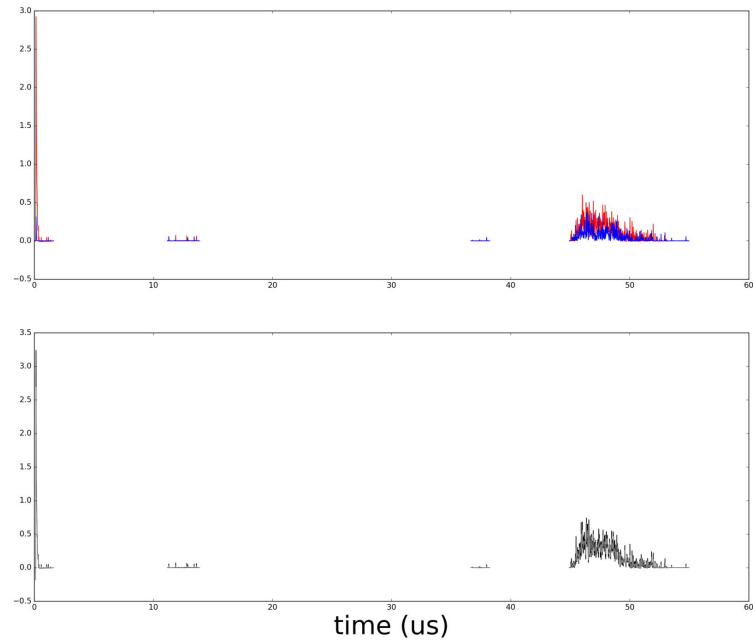
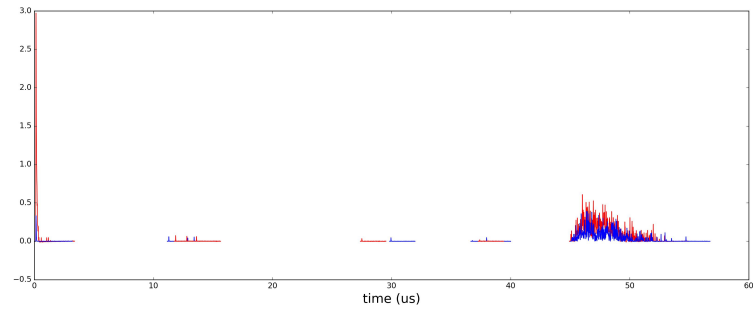
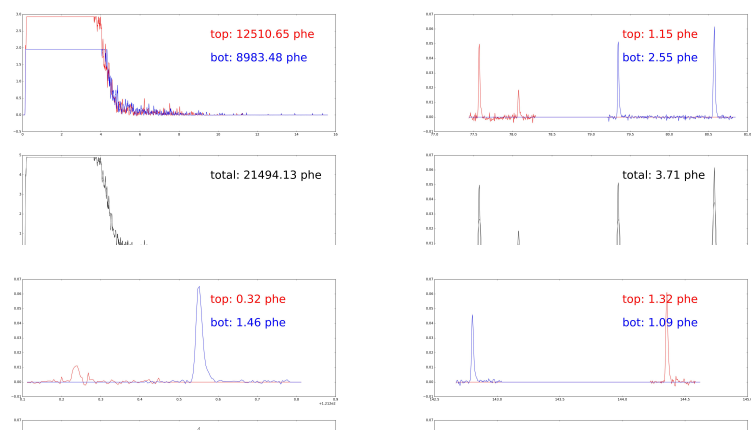
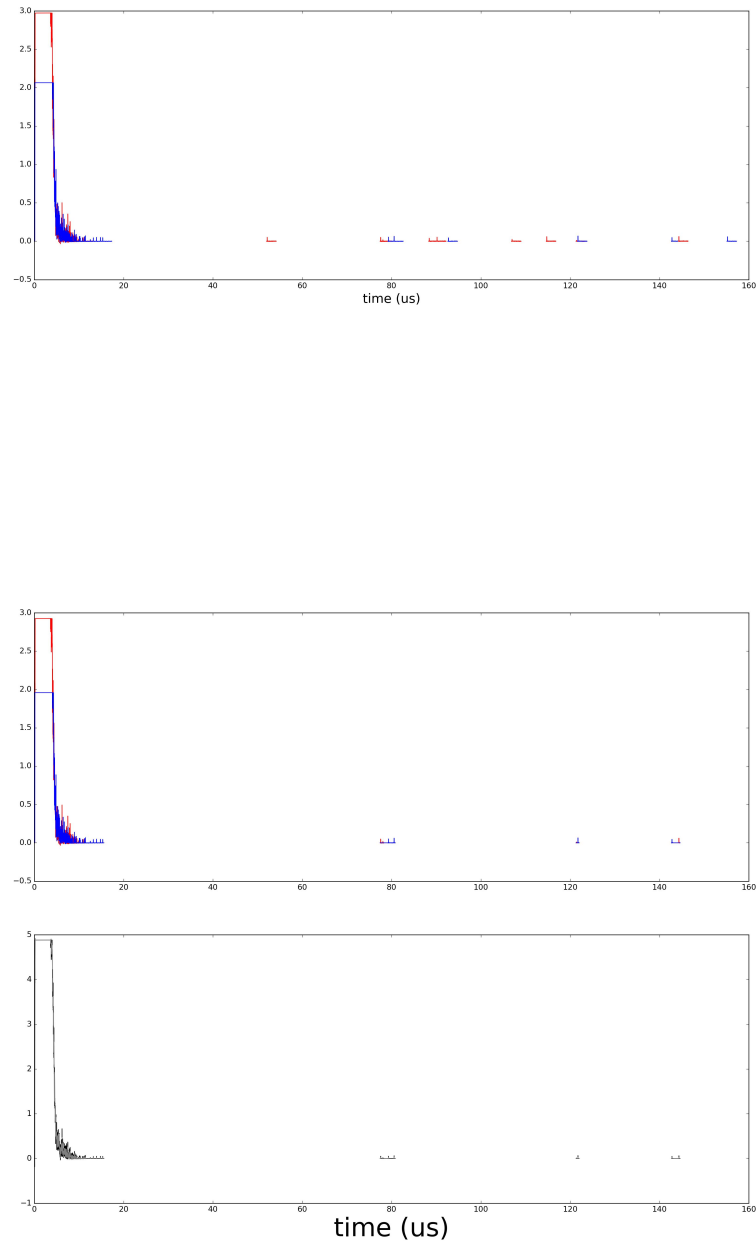


Figure 9.18: An S1 S2 event: S1 event(first 300ns) occurred outside the scintillation region and S2 event(rest), light created by electrons passing through the scintillation region. Red line is top PMT. Blue line is bottom PMT. Black line is the sum of the top and bottom PMTs.





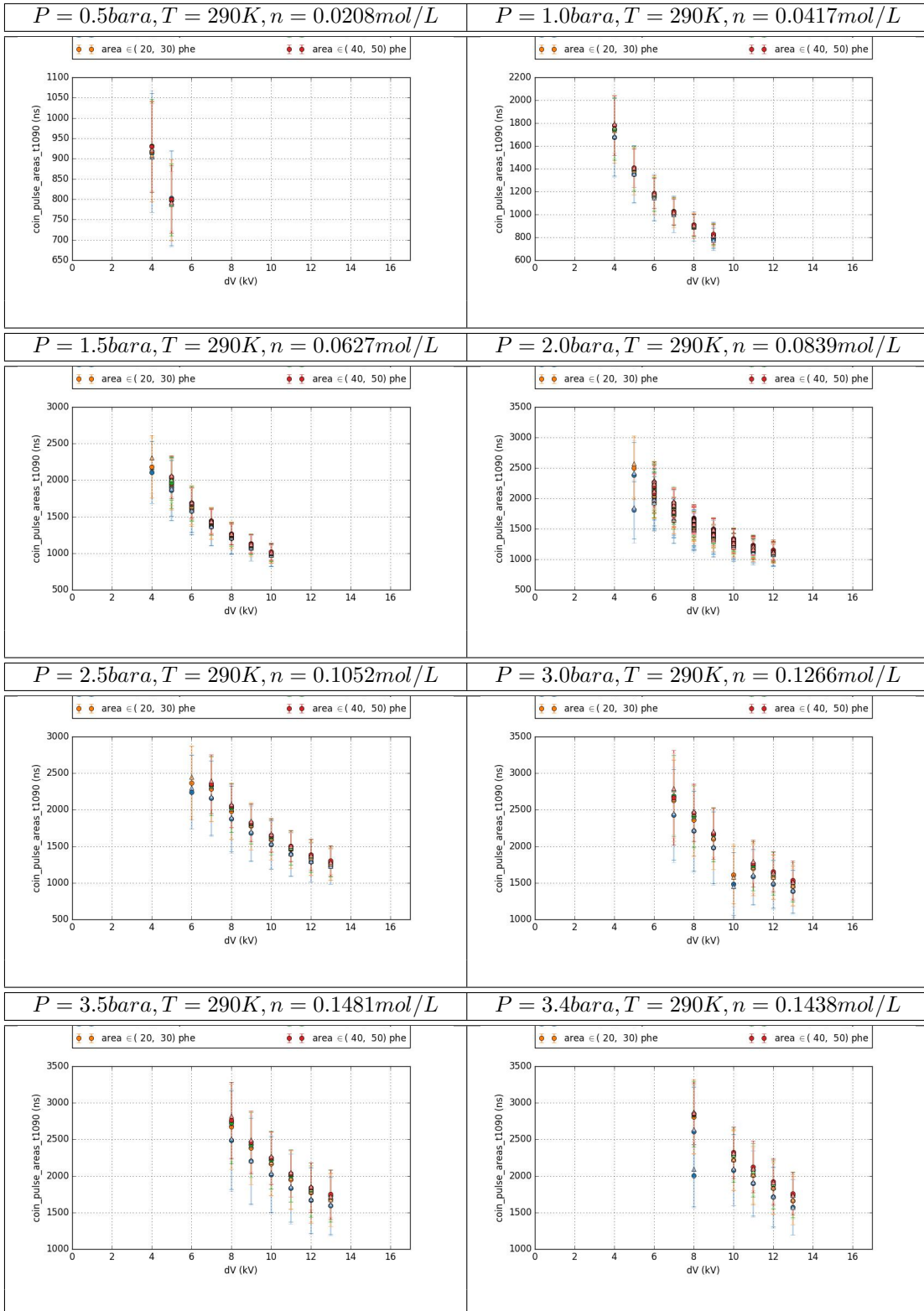


Figure 9.21: Measured time difference between 10% integrated area and 90% integrated area (t_{1090}). Solid circle: Mean and standard error. Triangle: Median and 14%, 86% percentile. Blue curve: 'coin_pulse_areas' $\in (10, 20]\text{phe}$. Orange curve: 'coin_pulse_areas' $\in (20, 30]\text{phe}$. Green curve: 'coin_pulse_areas' $\in (30, 40]\text{phe}$. Red curve: 'coin_pulse_areas' $\in (40, 50]\text{phe}$.

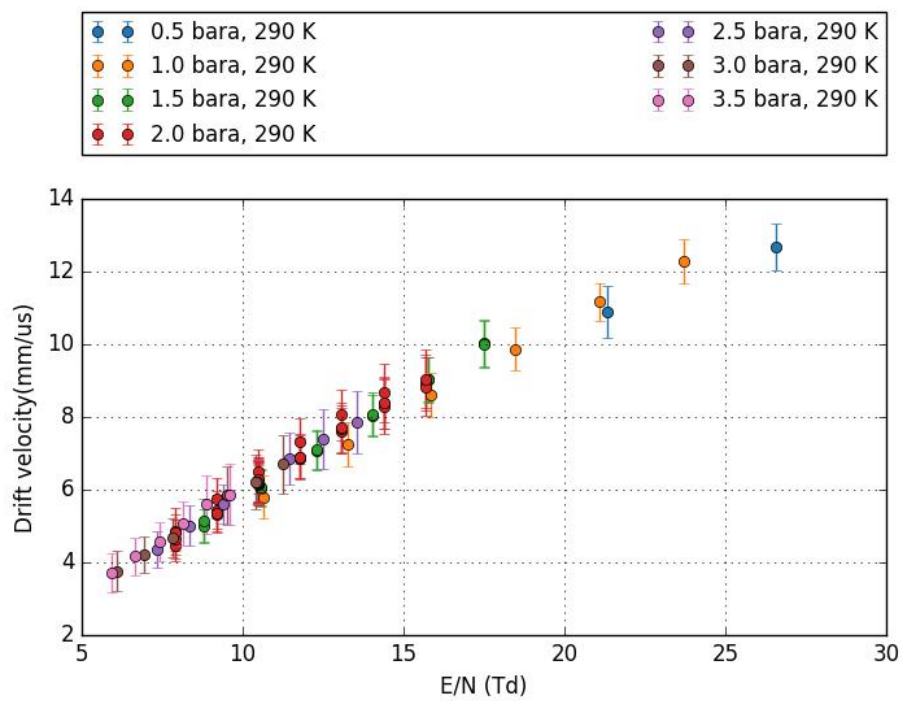


Figure 9.22: Drift velocity

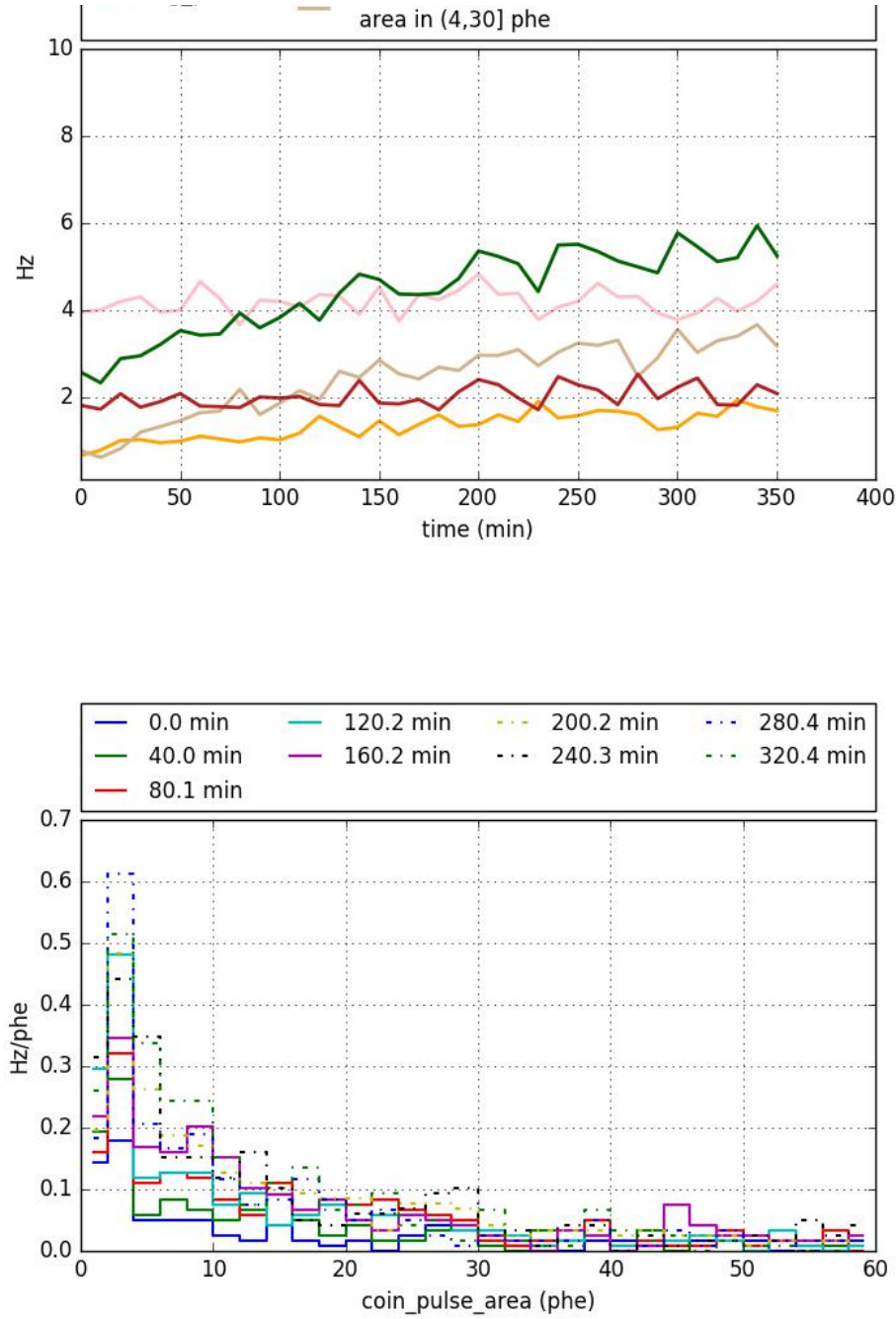


Figure 9.23: Top: emission rate changing over time during the experiment with $v_a = +4kV$, $v_g = -4kV$. orange: area $\in (0,4]$ phe, tan: area $\in (4,30]$ phe, red: area $\in (30,1000]$ phe, pink: area $\in (1000, \infty)$ phe, green: sum of tan and red curve. Bottom: emission rate at different area changing over time.

Chapter 10

EFT/IDM WIMP search with LUX

The second WIMP search in LUX (also usually referred as LUX WS2014-16) was performed between 2014 and 2016. This search improved the sensitivity on WIMP nucleon spin-independent cross sections from the first WIMP search performed at 2013 (LUX WS2013). The result of was published in 2017 [9]. As a supplement of the main WIMP search result, a separate study with the detail nuclear response was performed with the WIMP search data on a extended energy range. The study was using a Effective Field Theory(EFT) model for the nuclear response. This chapter describes the EFT analysis(EFTWS2014-16). It describes the data selection on the stability of this search. It describes the cuts for single scatter events and the cut efficiencies. It describes the background analysis. Finally, it describes the procedure for translating the WIMP search data into a EFT dark matter result.

10.1 Run stability

LUX detector was operated the TPC filled with Liquid xenon. The top, anode, gate, cathode, bottom grid electrodes were biased to -1, 7, 1, -8.5, -2 kV. This maintains the drift electric field between the gate and cathode grid at 60-400 kV/cm, and the extraction field was 7.5 kV/cm in gaseous xenon. The liquid level in LUX detector was maintain by the weir that is installed on the side of the TPC. Liquid xenon that exceed the height of the weir will flow out from the TPC region. This maintains the gas region thickness between the anode grid and the liquid xenon surface at 0.5 cm. The gas pressure of the TPC is 1.95 bar, and the temperature of the liquid xenon is 177 K. The variation of the temperature and pressure is less than 0.5 K and 0.01 bar. During the run, 118 PMTs were on recording. One of the PMT (PMT 26) is showing a slightly more unstable behavior

comparing to the other PMTs. The DAQ system was configured to trigger on S2 pulse [10]. After the trigger, the DAQ will open a $500\ \mu s$ acquisition window preceding the trigger time and a $500\ \mu s$ acquisition window succeeding the trigger time. This allowed both S1 and S2 pulse to be captured in the acquisition window, because the S1 and S2 pulse could have maximum time separation of $\sim 400\ \mu s$. The trigger was also compared with DAQ from outer detector water tank PMTs. Events potentially have external source are rejected. Data taking for WS was mostly continuous except for the interruption from weekly calibration from ^{83}Kr and other calibrations that happens less frequently.

In preparation for WS2014-16 exposure, the anode, gate and cathode grid electrodes were conditioned in cold xenon gas. During the conditioning, each electrode was maintained with a voltage that is just below its discharge voltage. The purpose of this conditioning was to improve the capability of applying higher voltages on each grid. This allowed us to have a higher electron efficiency at $0.73 \pm .04$ comparing to WS2013 at 0.49 ± 0.03 . However, this conditioning also burned the outer side of the PTFE panels on the radial boundary of the detector[11]. This caused the continuous charge deposition on the PTFE panel and altered the electric field in the detector on time and space. The full search are separated to 16 independent searches by time and space. The 16 results are combined to give the final limit.

10.1.1 General

LUX WS2014-16 was perform with WIMP search period and calibration period.

10.1.2 PMT

PMT 26

10.1.3 Light yield

The light yield of the TPC was studied from calibration with krypton 83 meta-stable state(^{83}Kr) source. The light yield model was further confirm with LUXSim, a Geant4 based simulation with LUX geometries, for optical propagation in LUX detectors.

10.1.4 Exposure time

Period of electron drift time smaller than $500\mu s$ are excluded from this analysis.

The exposure time of WS2014-16 was 332.0 live days. The expo

10.1.5 16 separate detectors

10.1.6 Summary

10.2 Cut and cut efficiency

A WIMP candidate event should statisfy:

- be an isolated event in time,
- be a single scatter event in the fiducial region in the TPC,
- not veto by coincidence with the Water Tank scintillation,
- have the shape and quanta of S1 and S2 pulse consistent with an NR.

Chapter 11

Overview of Dark Matter research

For the past few decades, dark matter has been an overwhelming interesting concept for the explanation for different aspects in cosmology. Dark matter could provide a single almost self sufficient theory to explain several observations in cosmology scale. It explains the history revolution of the universe, the predicted abundance of Hydrogen, Helium and other light elements from nucleosynthesis. It explains the amplitude of the temperature anisotropy spectrum in the cosmic microwave background(CMB), especially the ratio of the amplitudes and the relative ratios of the amplitudes of peaks. It also explains several observation in the formation of the different scale structures in the universe. Dark matter also could explain the observations in galactic scale. This includes the discrepancy in mass between luminescence(baryonic) mass and the weak lensing mass, as well as the weak lensing of CMB, the galactic rotation curves, etc. Several other observations including the abnormally at 3.5keV spectrum were also related to the existence of dark matter.

Based on the observation, people have proposed different ideas of the formation of dark matter. Non-relativistic(heavy mass) particle format dark matter(cold dark matter, CDM) has its advantage for the explanation for its nature abundance via freeze-out theory at the early stage of the universe and the low mobility for accumulating in cluster formation. However, relativistic particle dark matter is still being discussed, for its advantage in explaining the for explaining the formation of large scale structure, for example big supeer clusters and hollows at the scale of $50MPC$ in the space. And other format of dark matter, for example, massive astrophysical compact halo object(MACHO) including black holes or neutron stars as well as brown dwarfs and unassociated planets, may also explain the discrepancy of the mass quantity in the galaxy halo.

However, it might be dangerous to assume the same physics between the early days of the universe and now. And even though dark matter is a single nice explanation for several big phenomena, it cannot be excluded that several different explanations exist for these different problems.

In this chapter, I will review the existing evidence for dark matter. I will also discuss about the candidates for the format of dark matter particles/objects. I will not attempt to cover the full

history of both the observations and the detail mathematical calculations in this thesis. For those details, readers should refer to [12–14].

11.1 Cosmological evidence for dark matter

11.1.1 Evolution of the universe, density perturbation

According to most of the compelling theory and evidence of the evolution of the universe, the universe is expanding now. We are on the stage of the acceleration of the expansion of the universe. The rate of the expansion of the universe is guided by the density of the universe in the curvature space time. This lead to the famous Friedmann equations:

$$\frac{\dot{a}^2 + k}{a^2} = \frac{8\pi G\rho + \Lambda}{3} \quad (11.1)$$

$$\frac{\ddot{a}}{a} = -\frac{4\pi G}{3}(\rho + 3p) + \frac{\Lambda}{3} \quad (11.2)$$

Here, a is the scale factor that describes the coherent distance of the universe. Conventionally, a is taken to be 1 at the present time.

G is the Newton's gravitational constant(normal value is $6.67 \times 10^{-8} \text{cm}^3 \text{g}^{-1} \text{sec}^{-2}$).

Λ is cosmological constant.

k is the spatial curvature. If k is positive, the shape of the universe is hyperspherical. If k is negative, the shape of the universe is hyperbolic. And if k is zero, then the universe is flat. ρ , and p is are density and pressure of the universe.

\dot{a} , and \ddot{a} are the first and second order time derivatives of a .

The combination of the two Friedman equations lead

$$\ddot{\rho} = -3H(\rho + p) \quad (11.3)$$

The most simple model usually includes two types of components, radiative components(R), and non-relativistic matter components(M). With reparameterizing Freidmann equation, the cosmological constant term(Λ) can also be written in forms of density.

$$\rho_\Lambda = -p_\Lambda = \frac{\Lambda}{8\pi G} \quad (11.4)$$

$$(11.5)$$

$\rho_{,i}$ is used to demonstrate the density of i th component. The relationship between ρ and p for different components of the universe is depending on the thermal characteristic of the particle. With the assumptions of this relationship and the initial quantity of the density of the universe, one can

solve the equations 11.1 for $a(t)$ and the rate of the expansion of the space $H \equiv \frac{\dot{a}}{a}$. The current value of H , H_0 , is conventional called Hubble constant.

It is convenient to work with the critical density,

$$\rho_{cr} = \frac{3H_0^2}{8\pi G} \quad (11.6)$$

And for each component i , define the density parameter $\Omega_{,i} \equiv \frac{\rho_{,i}}{\rho_{cr}}$. The current value of $\Omega_{,i}$ is noted as $\Omega_{0,i}$. The density of radiation scales with a^{-4} , the density of matter scales as a^{-3} . The curvature term(K) can be written in $\Omega_{,K}$ by replacing

$$\Omega_{,K} \equiv -\frac{k}{H_0^2} \quad (11.7)$$

the Friedmann equations can be simplified as

$$\frac{H^2}{H_0^2} = \Omega_{0,R}a^{-4} + \Omega_{0,M}a^{-3} + \Omega_{0,K}a^{-2} + \Omega_{0,\Lambda} \quad (11.8)$$

In the following content, if not otherwise specified, short notation Ω_i is used for $\Omega_{0,i}$

The matter of the universe is separated to two parts, baryonic(B) and non-baryonic. The non-baryonic matter is usually called dark matter(DM).

$$\Omega_M = \Omega_B + \Omega_{DM} \quad (11.9)$$

The previous discussion shows the universe went through three major section. By the dominant fraction of mass component, they are called radiation dominant era, matter dominant era, and a dark energy (cosmology constant Λ) dominant era. These basic background knowledge would help the understanding of the cosmological evidence of the existence of dark matter.

11.1.2 Nucleosynthesis

The abundances of light elements in the universe, hydrogen, deuterium, helium, and lithium, is depending on the total baryon density of the universe. This section is based on the Big-Band nucleosynthesis review from [15]. Measurements of the abundances of light elements, especially the ratio between the abundances of different light elements can be used to provide an expect range of the baryon matter density. The fact that this baryon density measurement agrees with the prediction of the measurement of the power spectrum of CMB is remarkable.

The nucleosynthesis theory describes the creation of light elements. At the early stage of the

universe, shortly after the end of inflation, the temperature of the universe is hot, the particles in the universe are in a thermal equilibrium phase. Weak interactions exchanges neutron and proton. The density of the ratio between neutron and protons at temperature T is demonstrated by the

$$n/p = \exp\left(\frac{-(m_n - m_p)}{T}\right) \quad (11.10)$$

where m_n , and m_p is the mass difference between neutron and proton.

As temperature dropped, the neutron-proton conversion rate fell faster than the Hubble expansion rate. This departure from equilibrium(freeze-out), happened around $T_{fr} \sim 1 MeV$. And the neutron proton ratio at this time is around $\sim 1/6$. After freeze-out, the neutron could beta decay to proton until the temperature dropped significantly below the binding energy of deuterium, $\Delta_D = 2.22 MeV$. The photo dissociation by the high number density of photons delayed the formation of deuterium. The formation of nuclei is heavily sensitive to baryon photon ratio $\eta \equiv \frac{n_b}{n_\gamma}$.



The number density of photons per baryon, $\eta^{-1} \exp(-\frac{\Delta_D}{T})$, falls below unity at $T \sim 0.1 MeV$. Thus the start time of Deuterium formation t_D is related to η . Bigger η would result in an earlier formation of Deuterium and a high production of Helium 4. Since η is a small value, $\eta_{10} \equiv \eta \times 10^{-10}$ is normally used instead. The neutron proton ratio would drop to $\sim 1/7$ at this moment. Nucleosynthesis chain started to form deuterium and other light elements through nuclear reactions.

Nearly all neutrons turned into deuterium then ended up as 4He . Heavy nuclei did not form in significant quantity because of the absence of stable nuclei with mass number 5 and 8 and the large Coulomb barriers for nuclear reactions to overcome. Some of the chain nuclear reaction is also sensitive to photon density.

As the universe keep expanding, the density of the proton and neutron decrease. Once it fell low enough to halt the nuclei formation and nuclear reaction. All neutrons that is not bounded to a stable nuclei would decay to proton. Based on the evolution of the temperature and baryon density in the early stage of the universe, and the measured cross section of the nuclear reaction processes, the primordial element density can be estimated theoretically. The primordial element fractions were measured by observations of light spectra of the low-metallicity systems.

Figure ?? shows how the element abundances on baryon density. Based on the measurement of CMB, we know that the temperature of the photon today is $2.73 K$. So

$$\Omega_{b0} h^2 = 0.0037 \eta_{10} \quad (11.12)$$

where Hubble constant $H_0 = 100 h km \bullet s^{-1} \bullet Mpc^{-1}$ and $h = 0.5 - 0.8$ The overall concordance on the figure provides a measure of the baryon density $\Omega_B = 0.040 \pm 0.004(95\% CL)$ [16, 17]. This

value showed a great agreement with the measurement from the CMB. Both of them are together evidence for baryonic matter is not the only matter content in the universe.

11.1.3 The Cosmic Microwave Background

The strongest cosmological evidence for existence of dark matter comes from the power spectrum of the measurements of the anisotropies of the cosmic Microwave Background(CMB). People can refer to [15] for better understanding of the CMB.

The CMB is electromagnetic radiation in the universe at the epoch of recombination, approximately $t_{dec} \sim 380,000$ years after the big bang [18]. It is an almost perfect isotropic Planck black body radiation at $2.73K$. On top of the isotropic radiation, there are anisotropy features with amplitude 10^5 smaller than the amplitude of the isotropic components. The anisotropy features CMB provides evidence for the density fluctuation of the universe at the recombination epoch and evidence for dark matter.

The story of CMB start from the early stage of the universe. At that time the universe was opaque to photons due to the highly ionization medium in the universe. As the universe expand, the temperature of the universe eventually dropped below the ionization energy of an atom. Free electrons and nuclei combine into neutral atom. The universe became more transparent. Or in another word, photons started to decouple. This time is called recombination epoch. This transition region is also called the surface of photon last scattering. This "surface" is very "thin" in range of time, comparing to the duration of the life of universe before, and the relative temperature evolution is also small during that period. So the isotropic part of the photon spectrum look like a perfect Planck black body radiation. The expansion of the universe shift the wavelength of these photons with a redshift z , which is defined to be $a \equiv 1 - \frac{1}{a}$. The temperature of the recombination is $\sim 3000K$, corresponding redshift of $z = 1100$. The relic temperature of the photon radiation is $2.73K$, which is what we observe today.

Since the CMB reflects the photon emission at the small time range of recombination, it reveals the density fluctuation at that recombination time. This density fluctuation showed up in the anisotropic radiation spectrum. Figure ?? shows the measure power spectrum of the anisotropic radiation. The power spectrum is the result of fitting the fluctuation ratio of temperature $\frac{\delta T}{T}$ with spherical harmonics. The amplitude for each l indicates the Fourier transformation of the baryon density fluctuation. Smaller l on the power spectrum correspond to large scale structures fluctuation, which lately may evolve to large scale structures in the universe, super clusters and hollows etc. Larger l on the power spectrum correspond to small scale structures, which lately may evolve into small scale structures in the universe, galaxies, etc.

The growing of density fluctuation under gravity can be derived from the combination Newtonian gravity and fluid dynamics. With joining Euler fluid equation, fluid continuity equation, and Poission

equation of Newtonian gravity, one can derive the growing of density fluctuation δ_k .

$$\ddot{\delta}_k + 2\frac{\dot{a}}{a}\delta_k + \left(\frac{k^2 v_s^2}{a^2} - 4\pi G\rho\right)\delta_k \quad (11.13)$$

here δ_k is the Fourier transformation of $\frac{\Delta\rho}{\rho}$, $\Delta\rho$ and ρ are the density fluctuation and average density at certain moment.

v_s is the speed of sound wave. $v_s = \frac{\Delta P}{\Delta\rho} \sim \frac{1}{\sqrt{3}}$ for matter medium.

k_J is the wave number satisfies

$$\frac{k_J^2 v_s^2}{a^2} - 4\pi G\rho = 0 \quad (11.14)$$

For wave number $k \ll k_J$, 11.13 shows the solution of δ_k would not be stabilized by gravity. The corresponding comoving wavelength $\lambda_J = \frac{2\pi}{k_J}$ of k_J is called Jeans scale. Jeans mass M_J

$$M_J = \frac{4\pi\rho}{2} \left(\frac{\lambda_J}{2}\right)^3 \quad (11.15)$$

is the mass within Jeans scale. When the fluctuation scale exceeds Jeans scale or the mass contained in fluctuation exceeds Jeans mass, the system is not gravity stabilized.

11.13 shows during the radiation dominant, the growing of matter fluctuation is slow. After the radiation matter equilibrium time t_{eq} , matter start dominant, the growth of matter fluctuation scale proportional to a .

From the density fluctuation of today, $\delta \sim 1$, the derived density fluctuation at CMB time is $\sim 10^{-3}$. Comparing this value with the density fluctuation measured from the CMB, $\delta \sim 10^{-5}$, there is a clear discrepancy. This results in the proposing of dark matter. During the time between t_{eq} ($\sim 10,000$ years from the Big Bang) and t_{dec} , baryons were still strongly coupled with photons. This results a larger v_s for baryons. The growing of baryon density fluctuation is slower. At the same time, the growing dark matter density fluctuation is not influenced, still scales with a . The longer time for the density fluctuation to grow for dark matter results in a higher matter density fluctuation at the CMB time. This gives an explanation for the discrepancy.

The recent measured baryon density, cold dark matter density, and the derived matter density from Planck satellite are $\Omega_B h^2 = 0.02222 \pm 0.00023$, $\Omega_C h^2 = 0.1199 \pm 0.0022$, $\Omega_M = 0.315 \pm 0.017$ (with Hubble constant $h = 0.6726 \pm 0.0098$),?. This is a shocking result that showed the dominant component of matter in the universe is dark matter. The power spectrum shows a great fit with Λ CDM model, a universe with cold dark matter as the dark matter content. The discussion of cold dark matter and Λ CDM model will be in the next section.

11.1.4 Structure formation

From the previous discussion, we know that the clustering of the matter in the universe is the result of instability of gravity. The small density fluctuation in the early time of the universe would grow to big density fluctuation over time. The structure formation of different scale is highly related to the initial density fluctuation spectrum and the time when the related physical scale λ_f enter the event horizon $r_h(t) = \int_0^t \frac{1}{a(t')} dt'$. The great agreement between the simulations of the structure formation of the universe and the measurement of the structure formation of the real universe shows the advantage of cold dark matter and Λ CDM model.

Cold dark matter, warm dark matter[19], and hot dark matter are

In the freeze-out model, the dark matter particle(here after as X) interacts with standard model particles, and the dark matter particle with its anti particle annihilate to standard model particles. Both dark matter particles and standard model particles are both created and achieved an equilibrium state as the early stage of universe. As the universe expands, the annihilation rate of the dark matter particle, which scale as T^5 , dropped below the expansion rate, which scales as T^2 . After then, the dark matter density will instead essentially drop with expansion of the universe and contribute to a relic density today. The time that annihilation rate reach expansion rate is called the decouple time of the dark matter. The correspond temperature is noted as T_F .

Standard calculation for the relic density is estimated by the Boltzmann equation. The evolution of the number density of dark matter(n) can be written as([12], eq:15),

$$\frac{dn}{dt} + 3Hn = - <\sigma v> (n^2 - n_{eq}^2) \quad (11.16)$$

where σ is the total annihilation cross section, v is the velocity, and bracket denote the thermal average. n_{eq} is the number density at thermal equilibrium. For massive particles, one has Maxwell-Boltzmann approximation of

$$n_{eq} = g(\frac{mT}{2\pi})^{3/2} e^{-m/T} \quad (11.17)$$

where g is the degree of freedom.

$<\sigma v>$ can be approximate in powers of v^2

$$<\sigma v> = a + b <v^2> + \mathcal{O}(<v^4>) \approx a + 6b/x \quad (11.18)$$

where $x \equiv m/T$.

The solution of relic density today is ([12], eq 26)

$$\Omega_X h^2 \approx \frac{1.07 \times 10^9 GeV^{-1}}{M_{pl}} \frac{x_F}{g_* / a + 3b/x_F} \quad (11.19)$$

where g^* is the relativistic degree of freedom, x_F is the value of x at freeze out temperature.

For order of magnitude estimation, ([12], eq:28)

$$\Omega_X h^2 \approx \frac{3 \times 10^{-27} \text{cm}^3 \text{s}^{-1}}{\langle \sigma v \rangle} \quad (11.20)$$

Furthermore, if the mass of the dark matter particles are close to the mass of some standard model particles, the relic density can be changed by coannihilations, which is the resonance decay between the dark matter particles and standard model particles.

11.2 Galactic Evidence of dark matter

11.2.1 Galactic Rotation Curves

The galactic rotation curves are the almost earliest, and the most convincing observation results for the existence of dark matter. The measurement of the galactic rotation curves, which is the tangential velocity of stars about the galactic center as a function of their distance from the galactic center, show a plateau velocity after reach out a certain distance from the galactic center. As the acceleration due to gravity should go as $1/r^2$, the derived rotation velocity from the measurement of the luminous mass(stars, gas, nebulae, etc) is much lower than the plateau velocity [20]. This indicates that most galaxies are not composed primarily with luminous mass but with some other invisible mass. Oort[21] and Zwicky[22] separately gave the first measurement of this discrepancy. And this was the earliest hint of existence of dark matter relic in the galaxies.

From the rotation curves[] the radii of the range of dark matter is much larger than the luminous mass. This indicates the difference of between the baryons mass and dark matter. Baryons are capable of losing energy with radiation, so it is easier for them to lose energy, slow down and then cluster together. However, for dark matter, which is assumed to be collisionless particles that interact primarily by gravity, similar physics process would be in much rate. So that the average velocity of dark matter is higher. The total mass of the dark matter in most galaxies are 10 times higher than the luminous matter. However, this ratio has a variance between different type of galaxies, and different clusters. Because of the difficulty of measuring the mass in the center of the galaxies, it gains uncertainty for the distribution of the mass profile of dark matter in the galaxies. The most common model proposed for the mass profile by Navarro, Frenk, & White (1996, 1997, here after NFW),

$$\rho_{DM} = \frac{\delta_c \rho_{crit}}{(r/r_s)(1+r/r_s)^2} \quad (11.21)$$

where ρ_{crit} is the critical density of the universe, and δ_c and r_s are the concentration parameter and the scaled radius [23, 24].

An alternative explanation for the rotation curve is modified Newtonian dynamics(MOND) at low acceleration scale[25–27]. The theory is motivated by explaining the challenges in ΛCDM model [28].However, evidence supporting or rejecting this physics in lab has not been reported.

11.3 Other Observations

3.55keV annillation line observe for multiple galaxy X-ray spectrum

11.4 Evidence of Dark Matter

11.4.1

11.4.2 Gravitational lensing

11.4.3 Dark matter in clusters, galaxies

11.5 Dark matter candidates

11.5.1 Neutrinos

11.5.2 macho,super massive blackholes

11.5.3 WIMP

Chapter 12

Future overview of experiments for Dark Matter detection

12.1 LZ

12.1.1

12.1.2

12.2 Xenon100, Xenon-nT

12.2.1

12.2.2

12.3 DarkSide-50, DarkSide-20k

12.3.1

12.3.2

12.4 EXO, EXO200, nEXO

12.4.1

12.4.2

12.5 Other Liquid Xenon experiments, xmass,

12.5.1

12.5.2

12.6 Other Liquid Argon TPC Experiments, miniclean, mi-

Chapter 13

candidates and direct detection

The candidate are reviewed here[\[12\]](#)

Chapter 14

Gas Test descriptions

14.1 DAQ

14.2 Cuts

This section will discuss the pulse selection, aka cuts, that is used in *Gas Test* analysis. The purpose of this analysis is searching for electron emission pulses from the tested grid wires. Since electron emission pulse are in most situation rare in the detector, the pulse selection of these electron emission pulses is done conservatively. That is to keep as many candidate for electron emission pulse as possible.

A electron emission event should:

- be an isolated pulse in time, and
- have the correct pulse shape.

The evaluation of these cuts are done with simulations. The cut efficiency is defined as,

$$\text{cut efficiency} \approx \frac{\# \text{ pulse pass cut}}{\# \text{ simulations}} \quad (14.1)$$

Baseline found

Definition

Purpose

Method pulse area density in the 300 ns to 800 ns range is not low,

14.2.1 Summary of the cuts

To summarize the cuts that I used, to be an electron emission pulse candidate, a electron emission pulse candidate should satisfy these conditions:

- contains coincidence pulse in both PMTs,
- isolate from preceding pulses,
 - not have any preceding pulse in the previous $100 \mu\text{s}$,
 - not have any preceding large pulse in the previous 10 ms,
- have the correct pulse shape,
 - have more than one pod in at least one PMT,
 - not noise like,
 - not S1 like,
 - not muon like,
 - not S1 S2 like
 - not have pulse heavily concentrated only in one of the PMTs,
 - reduced pulse duration matches prediction from electron drift time between the gate and anode grids,
- not saturate any PMT (this is required for analysis with condition that gas pressure higher than 1 bara).

Chapter 15

Gas Test result

Appendix A

Calculation of voltage distribution in TPC

Electrostatic simulation for understanding the electric field distribution in the detector has been long evaluated. There are many software package that numerically solve this Poisson Partial Differential equation(PDE) problem using Finite Element Analysis(FEA) Method for given boundary condition. The common used softwares are, Matlab & Simulink, Elmer FEM solver, Maxwell, Comsol Multiphysics, etc. However, the cost of solving the exact problem using FEM is expensive, especially for 3 dimensional problems, or to get a more precise solution. The reason for is the size of problem grow very quickly as problem goes to 3d. However, this problem can be simplified in the detectors that are composed with simple reducible parallel segment, for example, most of the wire chambers, parallel TPCs. In this section we are going to talk about a method to estimate the electric field in these detectors.

A.1 Parallel-component detectors

The electric field equation of the space is solved by Poisson equation:

$$\nabla^2 \Phi = -\rho/\epsilon \quad (\text{A.1})$$

where $\rho = 0$, except for on the components or on the boundary. Suppose we have a detector with n parallel components. They are sequently residing in the space. From top to bottom is component 1, 2, ..., n . The thickness of the i th component is d_i . The position of the i th component is z_i . For a detector that is composed with simple parallel components, for example, wire planes, etched metal planes, if each component is distant away from the other components, we can separate the solutions for each components by dividing the problem to a Poisson electric field equation with one component



Figure A.1: An example of a detector with parallel components. The actual voltage of the i th component is $V_{,i}$, the effective voltage of the i th component is $V_{0,i}$, the effective electric field on the top side of the i th component is $E_{up,i}$, the effective electric field on the bottom side of the i th component is $E_{down,i}$, etc.

in each space and the voltage boundary condition on the conjunction.

Normally because of it is hard to directly control the charge distribution of each component, with most high voltage power supplies, the normal method to operate is to have a desirable voltage potential, we assume the voltage on the i th component is $V_{,i}$. However, because of the component, for example, wire plane, etched metal plane is not 100% occupying the plane, the voltage potential of the void plane is normally different of the voltage on the component. We assume the average potential of the i th plane, the effective voltage of the i th component is $V_{0,i}$, like in fig: A.1.

Because of there is no space charge between two neighbor components, the average electric on a plane parallel to the detector components between two neighbor components should be a constant. We call the average effective electric field on the top side of the i th component, $E_{up,i}$, the average effective electric field on the bottom side of the i th component is $E_{down,i}$. We should have

$$\mathbf{E}_{down,i} = \mathbf{E}_{up,i+1}. \quad (\text{A.2})$$

If the detector is big and infinite in size in x and y direction, or within each component there is a periodic pattern on x and y direction, from Gaussian's law, we can easily get that on the top and bottom boundary, which is far away from the detector components, the electric field only has z

direction components.

$$\mathbf{E}|_{top,i} = E_{up,i} \mathbf{e}_z \quad (A.3)$$

$$\mathbf{E}|_{bottom,i} = E_{down,i} \mathbf{e}_z \quad (A.4)$$

The relation ship between the effective voltage $V_{0,i}$ and the effective electric field on the top and bottom of detector component $E_{up,i}$, $E_{down,i}$ is

$$E_{down,i} * (z_{i+1} - z_i - d_i) = V_{i+1} - V_i. \quad (A.5)$$

If the thickness of each component d_i is small, the equation can be simplified as

$$E_{down,i} * (z_{i+1} - z_i) = V_{0,i+1} - V_{0,i}. \quad (A.6)$$

Then we take a look at a section with one component. We can separate the electric field in the space $\mathbf{E}(\mathbf{x})$ into two parts,

$$\mathbf{E}(\mathbf{x}) = E_{\parallel} \mathbf{x} + \mathbf{E}_{else}(\mathbf{x}) \quad (A.7)$$

where the uniformed electric field along the x axis with magnitude $E_{\parallel} = \frac{1}{2}(E_{down,i} + E_{up,i})$. We notice that this part has no contribution to the net charge on the detector component. Thus, its contribution to the difference between the actual voltage on the detector components and the effective voltage along the plane where the detector components is. The rest part of the electric field is \mathbf{E}_{else} . On the boundary on the top and the bottom of the section, it has new boundary conditions,

$$\mathbf{E}|_{top,\infty,i} = (E_{up,i} - \frac{1}{2}(E_{down,i} + E_{up,i})) \mathbf{e}_z, \quad (A.8)$$

$$\mathbf{E}|_{bottom,\infty,i} = (E_{down,i} - \frac{1}{2}(E_{down,i} + E_{up,i})) \mathbf{e}_z. \quad (A.9)$$

The solution of this problem with the detector component geometry and the new boundary condition is \mathbf{E}'_{else} .

If the detector component is thin, then the two separate solutions have the same boundary condition, which means $\mathbf{E}'_{else} = \mathbf{E}_{else}$. The electric field scales with the potential in the space. If the solution for the potential and the electric field are $V(\mathbf{x})$, $\mathbf{E}_{\mathbf{x}}$. The solution with the same space and a times the value of the electric field on the boundary are $aV(\mathbf{x})$, $a\mathbf{E}(\mathbf{x})$. Since from previous discussion we know that $E_{up,i} - E_{down,i}$ component has more contribution to the solution than $E_{up,i} - E_{down,i}$

component. So we have

$$\Delta V = V_{,i} - V_{0,i} \quad (\text{A.10})$$

$$\propto E_{up,i} - E_{down,i}. \quad (\text{A.11})$$

If the detector component has period conditions on the x, y plane with dimension p , the electric field and the potential in the space scale with this dimension p . The solution with in a space that is a times larger and the same value of the electric field are $V_{new}(a\mathbf{x}) = V(\mathbf{x})$, $\mathbf{E}_{new}(a\mathbf{x}) = \frac{1}{a}\mathbf{E}(\mathbf{x})$. So we have

$$\Delta V \propto p. \quad (\text{A.12})$$

So we can write

$$\Delta V \approx G(E_{up,i} - E_{down,i})p. \quad (\text{A.13})$$

Grid factor G is a function of the geometry of the detector component.

From Maxwell equations, we got the charge distribution on the detector components should follow

$$\nabla \bullet \mathbf{E} = \rho/\epsilon. \quad (\text{A.14})$$

So the charge on the detector component for a given area is

$$d\rho/ds = \epsilon E \quad (\text{A.15})$$

Because of the parallel component is usually not zero, so the charge distribution on the top and bottom side of the detector component is usually different. For a given area on the surface of the component, the charge difference between the top and the bottom side is roughly $\rho = \epsilon_0(E_{up,i} + E_{down,i})$.

The force on the detector component for a given area is

$$dF/ds = \rho E_{external} \quad (\text{A.16})$$

A.1.1 A single grid plane

The most common detector component is single grid plane. For a grid that is consist of infinitely thin wires along y axis on the $z = 0$ plane. which are uniformly separated by distance a , like fig

[A.2.](#) Assuming the electric field on the top and bottom boundary is symmetric and the values are

$$z \ll 0 : \quad \frac{1}{2}E_{dif} \quad (\text{A.17})$$

$$z \gg 0 : \quad -\frac{1}{2}E_{dif} \quad (\text{A.18})$$

The solution for this problem is

$$V(x) = \frac{1}{4\pi}aE_{dif} \ln[2(\cosh \frac{2\pi z}{a} - \cos \frac{2\pi x}{a})]. \quad (\text{A.19})$$

The effective voltage potential on the $z = 0$ plane is 0. If the dimension of the wires r is not negligible, the potential on the wire should be

$$V(x) \approx \frac{1}{4\pi}aE_{dif} \ln[2(1 + (\frac{2\pi z}{a})^2/2 - 1 + (\frac{2\pi x}{a})^2)/2] \quad (\text{A.20})$$

$$= \frac{1}{2\pi}aE_{dif} \ln \frac{2\pi r}{a}, \quad (\text{A.21})$$

where $r^2 = z^2 + x^2$. So the grid factor G is

$$G = \frac{1}{2\pi} \ln \frac{2\pi r}{a} \quad (\text{A.22})$$

And the average electric field on the surface of the wire E_{av} is

$$E_{av} = E_{dif} \frac{a}{2\pi r} \quad (\text{A.23})$$

the charge on the wire in a uniformly electric field $E_{||}$ is

$$d\rho/ds = \epsilon E_{||} \cos \theta \quad (\text{A.24})$$

So the overall charge on the wire should roughly be

$$d\rho/ds \approx \epsilon(E_{av} + E_{||} \cos \theta) \quad (\text{A.25})$$

The transparency of the grid T is the probability that an electron from infinity distance from the bottom of the grid drift passing the grid. The grid gains full transparency if the sign of the charge



Figure A.2: The geometry of a single grid plane, with spacing a .

on the grid wires are negative everywhere, which is

$$E_{av} - E_{\parallel} \geq 0 \quad (\text{A.26})$$

$$-(E_{up,i} - E_{down,i}) \frac{a}{2\pi r} - \frac{1}{2}(E_{up,i} + E_{down,i}) \geq 0 \quad (\text{A.27})$$

$$\frac{E_{down,i}}{E_{up,i}} \geq \frac{a + \pi r}{a - \pi r} \quad (\text{A.28})$$

A.1.2 A meshed grid plane

A meshed grid contains wires along different directions. A simple meshed grid is consist of two single grid planes, which has wires along two perpendicular directions.

The grid factor of this is calculated by simulations. We put up a geometry that has the smallest cell of periodic pattern, fig: A.6. The grid planes location in the middle. The top and bottom plane of the cell box are both 1cm from the grid plane. They as well as the wire grid itself are assign with separate voltages V_{top} , V_{bottom} and V_{grid} . $V_{top} = V_{bottom}$ to make the cell symmetric. E_{top} and E_{bottom} are read from the result. The effective voltage on the grid plane V_0 is

$$V_0 = V_{top} - E_{top} * 1\text{cm}. \quad (\text{A.29})$$



Figure A.3: The geometry of a meshed grid plane, with spacing a .

The grid factor G is

$$G = \frac{V_{grid} - V_0}{2E_{top}} \quad (\text{A.30})$$

The results of grid factor is in fig: A.4. The curve can be roughly approximated to

$$G = \frac{0.5247}{2\pi} \ln \frac{0.5247a}{\pi 0.7488d}, \quad (\text{A.31})$$

which is equivalent to the result of a grid plane with wire radius a factor of 0.7488 smaller and wire spacing a factor of 0.5247 smaller.

The effect of the top bottom ratio of the electric field are also studied by simulation with $V_{top} \neq V_{bottom}$. Results in fig: A.5 show that this effect is small. Thus the approximation method we used to calculate voltage in the detector is valid.

A.1.3 etched grid with triangle, square or hexagon pattern

Similar simulation with Comsol Multiphysics are done for etched grid with triangle, square or hexagon pattern, fig: A.7. Results on in fig: A.8.

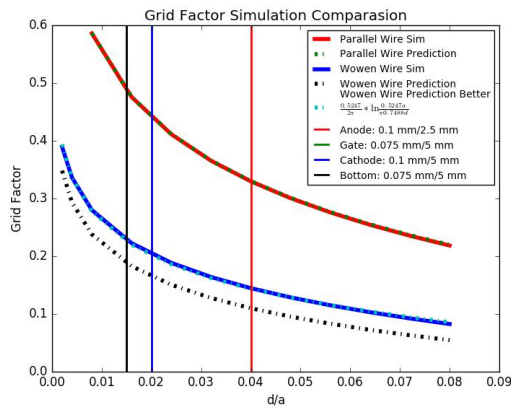


Figure A.4: The simulation result of grid factor for equal-spaced meshed grid.



Figure A.5: The simulation result how much is the effect of the top bottom ratio of electric field on grid factor for equal-spaced meshed grid.

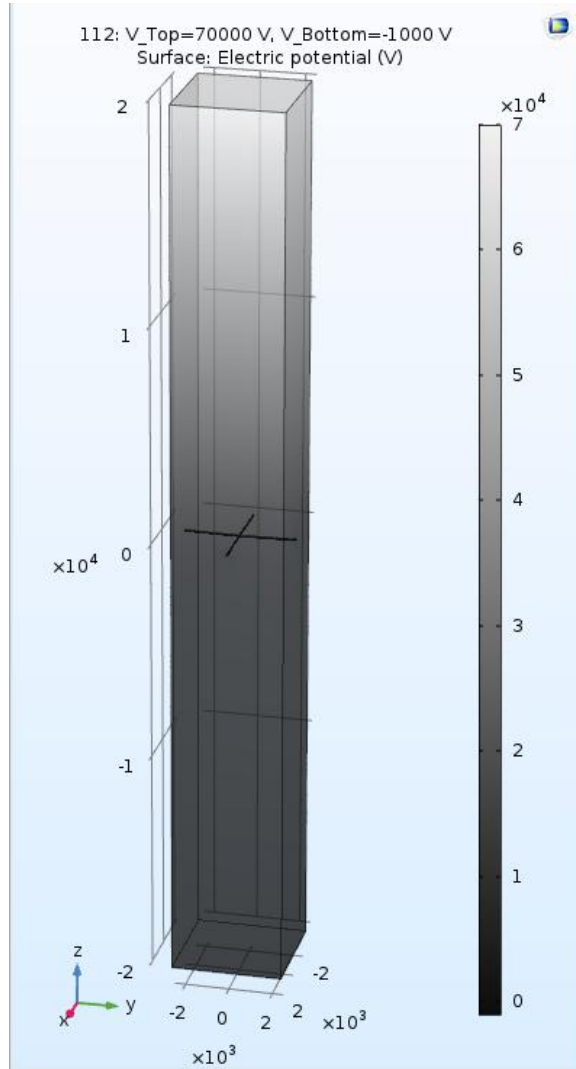


Figure A.6: A picture of Comsol simulationsimulation.

A.2 Deflection of the grid plane

Since charge on the grid component are also experience the Comlomb force. And this force will deflect the grid plane. It is important for us to know the deflection of the grid planes to get a better understanding of the potential distribution in the detector. There are many different method to estimate this. Here is the most common method.

This first method is called single wire calculation. For a uniformed rope with density of force per unit length λ . Assuming the tension of the end of the rope is T , and this tension should be the same along the rope.



Figure A.7: The geometry of an etched grid with triangle, square or hexagon pattern.



Figure A.8: The grid factor of an etched grid with triangle, square or hexagon pattern.

The curve of the rope underneath the force should balance this force with its tension, like fig: [A.9](#). It follow equations,



Figure A.9: The sagging rope.

$$T_{1x} = T_{2x} \quad (\text{A.32})$$

$$T_{1y} - T_{2y} = \lambda ds \quad (\text{A.33})$$

where ds is the length of the rope between x and x' , $ds = \sqrt{y'^2 + 1}dx$. Since $\frac{T_y}{T_x} = y'$,

$$T_x y'' dx = \lambda \sqrt{y'^2 + 1} dx. \quad (\text{A.34})$$

The solution is a catenary curve,

$$y = A \cosh \frac{x}{A}, \quad (\text{A.35})$$

$$A = \frac{T_x}{\lambda}. \quad (\text{A.36})$$

The catenary curve can be approximated by a parabolic curve.

$$y = \frac{1}{2A} x^2 \quad (\text{A.37})$$

So we get the famous sag formula, s is approximately

$$s = \frac{\lambda l^2}{8T} \quad (\text{A.38})$$

where l is the total horizontal distance between the two hanging points.

For a single grid with wire diameter d , spacing a and top bottom electric field E_{top} and E_{bottom} . The virtual work per unit area for moving the grid plane up a distance l is the changing of electric field energy, which is $\frac{1}{2}\epsilon(E_{top}^2 - E_{bottom}^2)l$. So the force density per unit area is $P = \frac{1}{2}\epsilon(E_{top}^2 - E_{bottom}^2)$. The force density per unit length λ is

$$\lambda = \frac{1}{2}\epsilon(E_{top}^2 - E_{bottom}^2)a \quad (\text{A.39})$$

Thus sag in the center should be,

$$s = \frac{1}{2}\epsilon(E_{top}^2 - E_{bottom}^2)a \frac{l^2}{8T} \quad (\text{A.40})$$

For a mesh grid with same spacing a on x and y direction. The wire density is twice the single grid, so the force is halved.

So the sag in the center should be,

$$s = \epsilon(E_{top}^2 - E_{bottom}^2)a \frac{l^2}{32T} \quad (\text{A.41})$$

The other method is called membrane method. We treat the full grid as a part of a big membrane sphere with radius R . This sphere is so big that the grid plane is a small section. For easiness of discussion, let's take a circle grid perimeter with radius R' . The force on unit area in a membrane, pressure on the membrane is P is the same as in previous discussion. The total force perpendicular to the perimeter line F' along the perimeter should contain in

$$F' \frac{R'}{R} = P\pi R'^2. \quad (\text{A.42})$$

For a grid plane, like , the total number of wire ends in the circle perimeter is $2 * 2R'/a$. If each wire is tension with force T , the total force perpendicular to the perimeter line is

$$F' = \sum T_i \cos \phi_i \quad (\text{A.43})$$

$$= \sum T \frac{l_i}{2R'} \quad (\text{A.44})$$

$$\approx 2T \frac{\pi R'^2/a}{2R'} \quad (\text{A.45})$$

$$= \frac{\pi T R'}{a} \quad (\text{A.46})$$

where ϕ_i is the angle between the line that connect the i th wire end and the membrane center and the i th wire. l_i is the length. The factor 2 comes from each wire has two ends.

So total deflection s which is calculated from the geometry of the sphere is,

$$s = \frac{R'^2}{2R} \quad (\text{A.47})$$

$$= \frac{aPR'^2}{2T} \quad (\text{A.48})$$

$$= \frac{1}{2}\epsilon(E_{top}^2 - E_{bottom}^2) \frac{al^2}{8T} \quad (\text{A.49})$$



Figure A.10: A membrane single grid plane.

With similar discussion the sag of a meshed grid should be half of the single grid plane.



Figure A.11

Appendix B

Error propagation discussion

The appendix is a discussion of the error propagation for

B.1 Bernoulli(Binomial) Process

There is N events, which N is not a fixed number. The expected value for the number of events is $E(N)$, and the variance of the number of events is $Var(N) = E(N^2) - E(N)^2$. Each event goes through a Binomial Process, which mean each event has the same probability of success p . The expected value and variance of the number of the successful event M is $E(M)$, $Var(M) = E(M^2) - E(M)^2$. M follows Bernoulli distribution,

$$M \sim B(N, p) \quad (\text{B.1})$$

. The probability mass function of $B(N, p)$ is,

$$Pr(M = k) = \binom{N}{k} p^k (1-p)^{N-k} \quad (\text{B.2})$$

for $k = 0, 1, \dots, N$.

$$\binom{N}{k} = \frac{N!}{k!(N-k)!} \quad (\text{B.3})$$

The expected value and variance of the number of the successful event is

$$E(M) = \sum_{N_i=1}^{\infty} P(N = N_i)P(M = k|N = N_i)k \quad (\text{B.4})$$

$$= \sum_{N_i=1}^{\infty} P(N = N_i)N_ip \quad (\text{B.5})$$

$$= E(N)p \quad (\text{B.6})$$

$$E(M^2) = \sum_{N_i=1}^{\infty} P(N = N_i)P(M = k|N = N_i)k^2 \quad (\text{B.7})$$

$$= \sum_{N_i=1}^{\infty} P(N = N_i)(N_ip(1-p) + (N_ip)^2) \quad (\text{B.8})$$

$$= E(N)p(1-p) + (E(N)^2 + Var(N))p^2 \quad (\text{B.9})$$

$$Var(M) = E(M^2) - E(M)^2 \quad (\text{B.10})$$

$$= E(N)p(1-p) + Var(N)p^2 \quad (\text{B.11})$$

The fraction of error is

$$\frac{Var(M)}{E(M)^2} = \frac{1}{E(N)} \frac{1-p}{p} + \frac{Var(N)}{E(N)^2}. \quad (\text{B.12})$$

B.2 Multiplication Process

There is another N events. Each event goes through a Multiplication Process. Each event has the same multiplication probability mass function. The expected value and variance of the number of the multiplication A is $E(A)$, $Var(A)$. M is the total number of multiplication.

$$M = \sum_{i=1}^N A_i \quad (\text{B.13})$$

where A_i is the number of the multiplication for the i th event.

$$E(M) = E\left(\sum_{i=1}^N A_i\right) \quad (\text{B.14})$$

$$= E(N)E(A) \quad (\text{B.15})$$

$$E(M^2) = E\left(\left(\sum_{i=1}^N A_i\right)^2\right) \quad (\text{B.16})$$

$$= E\left(\sum_{i=1}^N A_i^2 + \sum_{i \neq j} A_i A_j\right) \quad (\text{B.17})$$

$$= E(N(Var(A) + E(A)^2) + N(N-1)E(A)^2) \quad (\text{B.18})$$

$$= E(N)Var(A) + E(N^2)E(A)^2 \quad (\text{B.19})$$

$$= E(N)Var(A) + (Var(N) + E(N)^2)E(A)^2 \quad (\text{B.20})$$

$$Var(M) = E(M^2) - E(M)^2 \quad (\text{B.21})$$

$$= E(N)Var(A) + Var(N)E(A)^2 \quad (\text{B.22})$$

The fraction of error is

$$\frac{Var(M)}{E(M)^2} = \frac{1}{E(N)} \frac{Var(A)}{E(A)^2} + \frac{Var(N)}{E(N)^2}. \quad (\text{B.23})$$

If we replace $E(A)$ and $Var(A)$ with the expected value and variance of binomial process p and $p(1-p)$, we will get the same answer as last section. Consider two sequence multiplication process A and B , the expected value and variance of the final number of two sequence multiplication M is

$$E(M) = E(N)E(A)E(B) \quad (\text{B.24})$$

$$Var(M) = E(N)E(A)Var(B) + (E(N)Var(A) + Var(N)E(A)^2)E(B)^2 \quad (\text{B.25})$$

$$\frac{Var(M)}{E(M)^2} = \frac{1}{E(N)E(A)} \frac{Var(B)}{E(B)^2} + \frac{1}{E(N)} \frac{Var(A)}{E(A)^2} + \frac{Var(N)}{E(N)^2} \quad (\text{B.26})$$

If both A and B is binomial process with probability of success p_A, p_B .

$$E(M) = E(N)(p_A p_B) \quad (\text{B.27})$$

$$\frac{Var(M)}{E(M)^2} = \frac{1}{E(N)p_A} \frac{p_B(1-p_B)}{p_B^2} + \frac{1}{E(N)} \frac{p_A(1-p_A)}{p_A^2} + \frac{Var(N)}{E(N)^2} \quad (\text{B.28})$$

$$= \frac{1}{E(N)} \frac{p_A p_B (1 - p_A p_B)}{(p_A p_B)^2} + \frac{Var(N)}{E(N)^2} \quad (\text{B.29})$$

$$= \frac{1}{E(N)} \frac{1 - p_A p_B}{p_A p_B} + \frac{Var(N)}{E(N)^2} \quad (\text{B.30})$$

which is equivalent to a binomial process with the probability of success p_{APB} . Similarly, for k sequence multiplication proces $A_i, i = 1, 2, \dots, m$

$$E(M) = E(N) \prod_{i=1}^k E(A_i) \quad (\text{B.31})$$

$$\frac{Var(M)}{E(M)^2} = \frac{1}{E(N)} \sum_{i=1}^k \frac{1}{\prod_{j=1}^{i-1} E(A_j)} \frac{Var(A_i)}{E(A_i)^2} + \frac{Var(N)}{E(N)^2} \quad (\text{B.32})$$

Appendix C

Binomial likelihood discussion

If we measure a sequence of events, that we know is drawn from a Bernoulli distribution. How would we estimate the probability of the Bernoulli distribution p ? Assuming measuring this Bernoulli experiment N times, and the result is $X_1 = x_1, \dots, X_N = x_n$. Among these events, value 1 happen m times. Then the probability for this result to happen if p is the Bernoulli probability is

$$P(X_1 = x_1, \dots, X_N = x_n | p) = p^m (1 - p)^{N-m} \quad (\text{C.1})$$

According to Bayes Rules,

$$P(A|B) = \frac{P(B|A)P(A)}{P(B)} \quad (\text{C.2})$$

,

$$P(p | X_1 = x_1, \dots, X_N = x_n) = \frac{P(X_1 = x_1, \dots, X_N = x_n | p)P(p)}{P(X_1 = x_1, \dots, X_N = x_n)} \quad (\text{C.3})$$

The probability of $P(X_1 = x_1, \dots, X_N = x_n)$ is a constant unrelated to p . The probability of $P(p)$ would also be a constant if we know no further information,

$$f(p) = 1, \quad p \in [0, 1] \quad (\text{C.4})$$

Combining C.1, C.3, C.4, we get

$$P(p | X_1 = x_1, \dots, X_N = x_n) \propto P(X_1 = x_1, \dots, X_N = x_n | p) \quad (\text{C.5})$$

Considering the normalization of probability, we get

$$P(p|X_1 = x_1, \dots, X_N = x_n) = \frac{p^m(1-p)^{N-m}}{\int_0^1 dp \ p^m(1-p)^{N-m}} \quad (\text{C.6})$$

Maximum of this probability, we get

$$\max_p P(X_1 = x_1, \dots, X_N = x_n|p) = \max_p p^m(1-p)^{N-m} = \frac{m}{N} \quad (\text{C.7})$$

Expected value of p give $X_1 = x_1, \dots, X_N = x_n$,

$$E(p|X_1 = x_1, \dots, X_N = x_n) = \frac{\int_0^1 dp \ p \ p^m(1-p)^{N-m}}{\int_0^1 dp \ p^m(1-p)^{N-m}} = \frac{1+m}{2+N} \quad (\text{C.8})$$

$$\lim_{m,N \rightarrow \infty} E(p|X_1 = x_1, \dots, X_N = x_n) \approx \frac{m}{N} \quad (\text{C.9})$$

Variance of p give $X_1 = x_1, \dots, X_N = x_n$,

$$\begin{aligned} Var(p|X_1 = x_1, \dots, X_N = x_n) &= E(p^2|X_1 = x_1, \dots, X_N = x_n) - E(p|X_1 = x_1, \dots, X_N = x_n)^2 \\ &= \frac{\int_0^1 dp \ p^2 \ p^m(1-p)^{N-m}}{\int_0^1 dp \ p^m(1-p)^{N-m}} - \left(\frac{\int_0^1 dp \ p \ p^m(1-p)^{N-m}}{\int_0^1 dp \ p^m(1-p)^{N-m}} \right)^2 \\ &= \frac{(1+m)(1+N-m)}{(2+N)^2(3+N)} \end{aligned} \quad (\text{C.10})$$

$$\lim_{m,N \rightarrow \infty} Var(p|X_1 = x_1, \dots, X_N = x_n) \approx \frac{m(N-m)}{N^3} = \frac{\frac{m}{N}(1-\frac{m}{N})}{N} \quad (\text{C.11})$$

We realize that the probability expected value is not exactly equal to m/N , which maximized the likelihood function and also is the mean value of the results. Variance is not exactly $m/N(1-m/N)/N$. This is because the origin guess for we have p is uniformly distributed between 0 and 1. We can not eliminate the small probabilities for value of p deviated a lot from expected value.

Appendix D

Cryogenic and flow system in liquid xenon detector

D.1 Thermosyphon

D.2 heater PID

D.3 Heat exchanger

D.4 circulation system

panel, compressor, getter, etc weir

D.5 wave

D.6 bubble

Appendix E

Sensors

E.1 Level sensors

For a fluid system, we often need to know the liquid level or relative liquid level in different locations in the system. There are many ways to measure this, we will introduce a few that we used.

E.1.1 Differential pressure

The first way to measure liquid level or liquid level difference is using the differential gas pressure. If two gas space A and B are connected with static liquid with density ρ , then the liquid level difference

$$h_A - h_B = \frac{P_B - P_A}{\rho g} \quad (\text{E.1})$$

$$\approx \frac{P(\text{mbar})}{\rho(g/cm^3)} \text{cm.} \quad (\text{E.2})$$

This method is also used to measure the absolute liquid level by measuring the differential gas pressure on the top and bottom the liquid space. It is easier to measure the pressure on the top. However, it is a little different to measure the pressure on the bottom. The common method is to put a special drain unit on the bottom of the liquid space which allow fluid to flow through this drain when the amount of fluid is minimized. The drain is then usually connected to a thin tube that is heated up to evaporate the liquid that is contained in this tube, fig E.1. The gas pressure difference measured indicates the liquid level. This method is commonly used to



Figure E.1: A simple diagram of a differential pressure level sensor.

E.1.2 Capacitance

The dielectric liquid filling in the space in a capacitor would change its capacitance.

We designed several different type of capacitance level meters. The first type is called a vertical plate level sensor. As described in the name, the capacitor is consist with two parallel plates that is perpendicular to the liquid surface, fig: E.2. The plates have effective width w and the distance between two plates is d . The dielectric constant of the fluid is ϵ_l . The dielectric constant of the gas is ϵ_g , which usually is close to 1. The capacitance change with liquid level moving up a distance of h is

$$\Delta F = (\epsilon_l - \epsilon_g)\epsilon_0 \frac{wh}{d} \quad (\text{E.3})$$

$$\approx (\epsilon_l - 1) \frac{w(cm)h(mm)}{d(cm)} * 8.854 * 10^{-3} pF \quad (\text{E.4})$$

The second type, a horizontal plate level sensor is similar to the vertical plate one but with the two plates parallel to the liquid surface. The effective area of the capacitor is A . The capacitance with liquid level h_1 ($0 \leq h_1 \leq d$) above the bottom plate is

$$F = \frac{1}{\frac{h_1}{\epsilon_l \epsilon_0 A} + \frac{d-h_1}{\epsilon_g \epsilon_0 A}} \quad (\text{E.5})$$

$$= \frac{\epsilon_0 A}{h_1/\epsilon_l + d - h_1} \quad (\text{E.6})$$

So the capacitance change with liquid level moving up a distance of h is

$$\Delta F \approx \frac{\epsilon_0 A}{(h_1/\epsilon_l + d - h_1)^2} (1 - 1/\epsilon_l) h \quad (\text{E.7})$$

For a capacitor with effective area $A \sim \text{cm}^2$, plate distance $d \sim \text{cm}$, the capacitance change $\Delta F \sim 0.1\text{pF}$.

The third type is parallel wire level sensor. This type of level sensor has two thin parallel wires

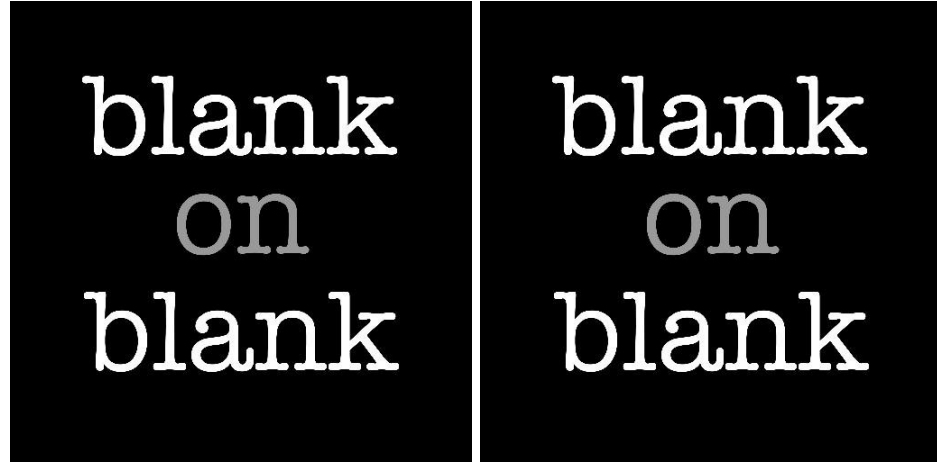


Figure E.2: A simple diagram of a vertical plate level sensor and a horizontal plate level sensor.

with radius a , and the distance between two wires is d , fig: [E.3](#). The capacitance change with liquid level moving up a distance of h is

$$\Delta F = \frac{\pi(\epsilon_l - \epsilon_g)\epsilon_0 h}{\arccos h \frac{d}{2a}} \quad (\text{E.8})$$

$$\approx \frac{\pi(\epsilon_l - 1)\epsilon_0 h}{\ln\left(\frac{d}{2a} + \sqrt{\frac{d^2}{4a^2} - 1}\right)} \quad (\text{E.9})$$

$$(E.10)$$

For a case with $\epsilon_l = 2$, $\frac{d}{2a} = 5$, $\Delta F \approx 0.1h(\text{cm})\text{pF}$. We notice that the capacitance is normally in 0.1pF range, which is very small to measure. A method to measure this capacitance is measure its relevant value to a reference capacitance. In the circuit the relaxation time of an RC circuit is measured with the reference capacitance and the unknown capacitance. Since relaxation time $\tau \propto RC$, the ratio of the relaxation time is the ratio of the capacitance between the unknown capacitance and the reference capacitance.



Figure E.3: A simple diagram of a parallel wire level sensor. The radius of the two wires are a . The distance between two wires is d .

E.2 Temperature sensor

We use many method to measure the temperature in the system, for example, gas pressure, resistance temperature detectors, thermocouples.

First method is using the gas thermal property. Known from thermodynamic, gas(fluid) quantity , temperature and pressure are related. So we can use two of them to derive the third. Normally gas quantity can be measured with flow meter, pressure can be measured with pressure gauge. And on the gas liquid saturation curve, temperature is a singly dependent of the gas pressure. So we can use the gas pressure to derive the gas/liquid temperature in the system. The second method is using Resistance temperature detectors (RTDs). RTD is a device that is made with material the resistance of which change with temperature. Actually most material has this property. However, because of the cost and sensitivity requirement, RTD materials are typically chosen to be platinum, nickel, or copper, which has big temperature coefficient and low cost. Especially, platinum RTD PT100 is one of the most common used one in the lab, 100 indicates its resistance at 0 degree Celsius is 100Ω . The temperature coefficient of resistance α , which is the fraction of resistance changing per Kelvin comparing to 0 degree Celsius. For pure platinum, $\alpha = 0.003925\Omega/(\Omega K)$, the industrial used platinum sensor, which $\alpha = 0.00385\Omega/(\Omega K)$. There are several standards specifies the accuracy of the RTDs. The most two are DIN EN 60751 (According to IEC 60751) in Europe and ASTM E1137 in North America.

RTD could be in forms of a wire, thin-film or other. The temperature sensitive material is normally

mechanically assembled or electroplating or spattering on a ceramic substrate. The precision of the measurement of temperature requires precision of the measurement of resistance. There are two issues for this measurement. First, long connecting wires are sometimes needed from the RTD and the readout circuit, and the resistance of the long wires are not negligible. Second, the contact resistance of the connectors between the RTD and the readout circuit can change the resistance of the connection wires each time. And choosing different wiring circuit can reduce the error of measurement. There are 2-wire, 3-wire, 4-wire RTDs, which is distinguished by the measurement circuit and the number of connection leads from the RTD.

The 2-wire RTD is only used when high accuracy is not required. The circuit is show in fig E.4. Sometimes, a Wheatstone bridge circuit is used to measure the resistance. As shown in the figure, the resistance of the connecting wires is added to that of the sensor. The error from the lead

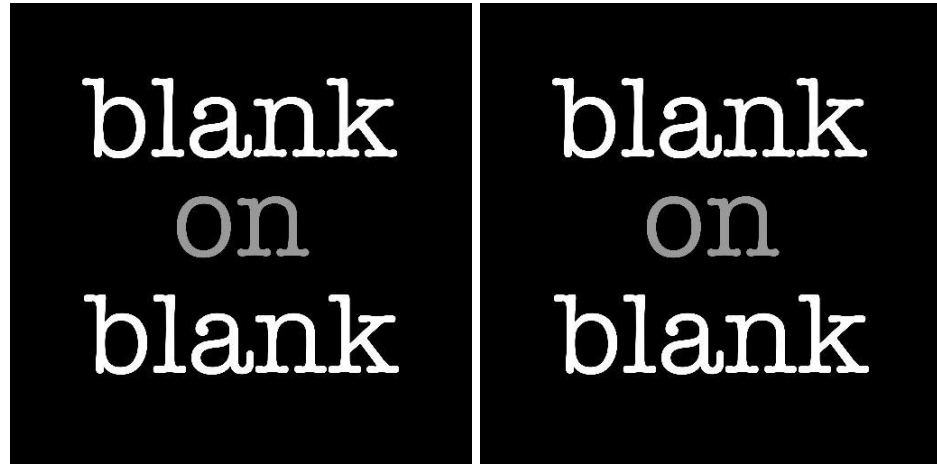


Figure E.4: The circuit for 2-wire RTD.

resistance, which is the combination of contact resistance and the wiring resistance, can be reduced by adding a third wire. Normally it is possible to choose the assembly of the RTD sensors so that the resistance of the leads are roughly matched in value between different wires. And this makes it possible to either estimate the value of the lead resistance or reduce the error that goes into RTD resistance.

Fig: E.5 shows a simple 3-wire circuit. R_T is the RTD sensor resistance. R_L is the lead resistance. The resistance between lead 1 and lead 2 $R_{12} = 2R_L$. The resistance between lead 1 and lead 3 $R_{13} = 2R_L + R_T$. So $R_T = R_{13} - R_{12}$. Fig: E.6 shows a circuit that cancels the effect of lead resistance with two constant current supplies. I_1 and I_2 are the current from the two current supplies. From the figure, the measured voltage U satisfies,

$$U = -I_1 R_{L1} + I_2 R_{L2} + I_2 R_T. \quad (\text{E.11})$$

If choosing $-I_1 R_{L1} + I_2 R_{L2} = 0$ (or roughly $I_1 = I_2$),

$$R_T = \frac{U}{I_2}. \quad (\text{E.12})$$

Fig: E.7 shows a method to measure with a 3-wire Wheatstone bridge. In the figure, the balance resistance $R_3 \sim R_T$ is chosen. The measured voltage U is

$$U = \frac{R}{2R} V_S - \frac{R_3 + R_L}{R_3 + R_L + R_T + R_L} V_S \quad (\text{E.13})$$

$$\Rightarrow R_T = R_3 \frac{V_S + 2U}{V_S - 2U} + R_L \frac{4U}{V_S - 2U} \quad (\text{E.14})$$

Since with balance Wheatstone bridge, $U \ll V_S$, the contribution to the error of R_T from the R_L term is small.

The 3-wire RTD is commonly used in industries and labs. Comparing to 2-wire RTD, 3-wire RTD significantly improves the precision. And 3-wire RTD requires less wires comparing to 4-wire RTD, which could be a saving of cost.



Figure E.5: The circuit for 3-wire RTD.

The most accurate circuit is 4-wire RTD circuit, which has no error contribution from the lead resistance. Fig: E.8. It requires only one constant current supply. It avoids the difficulty to balance



Figure E.6: The circuit for 3-wire RTD.



Figure E.7: The circuit for 3-wire RTD.

the Wheatstone bridge. And the RTD resistance is simply,

$$R_T = \frac{U}{I}. \quad (\text{E.15})$$

This relationship is valid even if the resistance of the four lead wires are different. So the measurement would be altered by each time connecting and disconnecting the device. Because of this reason, it is the most common used way to configure lab accuracy temperature sensors.



Figure E.8: The circuit for 4-wire RTD.

Appendix F

Gas Test RQ list

This chapter summarize the definitions of the RQs that is used for analysis in *Gas Test* analysis.

RQ name	shape	type	unit	default
'aft_tXX'	array (L,)	float32	ns	nan
	Time since the start time of the pulse till the integrated pulse area reach XX% of the total area of pulse. XX=05,25,75,95.			
'aft_t0', 'aft_t1', 'aft_t2'.	array (L,)	float32	ns	nan
	equivalent to 'aft_t01', 'aft_t50', 'aft_t99'.			
'arearq'	scalar	string		'waveareas_trim_end'
	RQ used to compute coincidence pulse area.			
'baselines'	array (L,)	float32	mV	nan
	Pulse baseline voltage.			
'channels'	array (L,)	uint32		
	Pulse channel number.			
'coin_pulse_amplitudes'	array (N,C)	float32	mV	nan
	Coincidence pulse amplitudes in each channel.			
'coin_pulse_amplitudes_neg'	array (N,C)	float32	mV	nan
	Coincidence pulse negative amplitudes in each channel.			
'coin_pulse_areas'	array (N,C)	float32	mV ns	nan
	Coincidence pulse areas in each channel.			
'coin_pulse_areas_neg'	array (N,C)	float32	mV ns	nan
	Coincidence pulse negative areas in each channel.			
'coin_pulse_areas_norm'	array (N,C)	float32	phe	nan

Continued on next page

RQ name	shape	type	unit	default
	Coincidence pulse area in each channel.			
'coin_pulse_areas_post_TTus'	array (N,C)	float32	phe	0
	Pulse area of TT us after the stop time of a coincidence pulse. TT=100,50,20,10.			
'coin_pulse_areas_pre_TTus'	array (N,C)	float32	phe	0
	Pulse area of TT us before the start time of a coincidence pulse. TT=100,50,20,10.			
'coin_pulse_areas_sum'	array (N,)	float32	phe	nan
	Coincidence pulse total area.			
'coin_pulse_areas_tXX'	array (N,)	float32	ns	nan
	Time since the start time of the coincidence pulse till the integrated coincidence pulse area reach XX% of the total area of the coincidence pulse. XX=01,05,10,15,25,75,85,90,95,99.			
'coin_pulse_areas_tXXYY'	array (N,)	float32	ns	nan
	'coin_pulse_areas_tYY'-'coin_pulse_areas_tXX'			
'coin_pulse_chs'	array (N,10)	int32		-1
	First 10 individual pulse channels in the coincidence pulse.			
'coin_pulse_ids'	array (N,10)	int32		-1
	First 10 individual pulse ids in the coincidence pulse.			
'coin_pulse_lastpulse_areas'	array (N,C)	float32	mV ns	nan
	Pulse area of the last pulse before a coincidence pulse in each channel.			
'coin_pulse_lastpulse_ids'	array (N,C)	int32		-1
	Pulse id of the last pulse before a coincidence pulse in each channel.			
'coin_pulse_lastpulse_lens'	array (N,C)	float64	ns	nan
	Pulse length of the last pulse before a coincidence pulse in each channel.			
'coin_pulse_lastpulse_times'	array (N,C)	float64	ns	nan
	Start time of the last pulse before a coincidence pulse in each channel (since LZ_EPOCH_DATETIME).			
'coin_pulse_lens'	array (N,)	float64	ns	nan
	Coincidence pulse length.			
'coin_pulse_times'	array (N,)	float64	ns	nan

Continued on next page

RQ name	shape	type	unit	default
	Coincidence pulse start time (since LZ_EPOCH_DATETIME).			
'coin_pulse_waveforms'	list (N,C,W)	float32	mV	0
	Waveforms of a coincidence pulse in each channel.			
'coin_pulse_waveforms_norm'	list (N,C,W)	float32		0
	Waveforms of a coincidence pulse in each channel normalize by single photo electron size.			
'coin_pulse_waveforms_sum'	list (N,W)	float32		0
	Sum of waveforms of a coincidence pulse in all channels normalize by single photo electron size.			
'coin_pulse_wtime_tXXYY'	array (N,)	float32	ns	nan
	Pulse height(h_i) weighted average of time(t_i) between 'coin_pulse_areas_tXX' and 'coin_pulse_areas_tYY'. XXYY=1585. $\bar{t} = \sum h_i t_i / \sum h_i$.			
'coin_pulse_wtimeN_tXXYY'	array (N,)	float32	ns^N	nan
	$\sum h_i(t_i - \bar{t})^N / \sum h_i$. XXYY=1585. N=2,3,4.			
'disp'	scalar	string		
	Display string 'a:va;g:vg'. (ex: 'a:+6.5;g:-6.5'.)			
'duration'	array (F,)	float64	s	
	Duration of a file.			
'dv'	scalar	float32	kV	
	Voltage difference between the anode grid and the gate grid.			
'evtnum'	scalar	int64		
	Number of all computed pulses.			
'in_coin_pulse'	array (L,)	bool		false
	Whether a pulse is in a coincidence pulse.			
'neg_area_fraction'	array (L,)	float32		nan
	Ratio of negative pulse area and the sum of positive and negative pulse area.			
'number_of_channels'	scalar	int32		4
	Number of channels.			
'pos_area_above_threshold'	array (L,)	float32	mV ns	
	Pulse area above a certain threshold (default: 2.5 mV).			
'pos_len_above_threshold'	array (L,)	float32	ns	
	Pulse length above a certain threshold (default: 2.5 mV).			

Continued on next page

RQ name	shape	type	unit	default
'pos_len_above_threshold_percentile_XX'	array (L,)	float32	ns	
				XX percentile above a certain threshold. XX=05,50,95.
'posareas'	array (L,)	float32	mV ns	
				Pulse positive area.
'post_baseline'	array (L,)	float32	mV	
				Pulse baseline computed from the end of the pulse.
'post_pulse_length'	scalar	float64	ns	1800
				Pulse length not used in the end of a waveform for coincidence pulse searching.
'pre_baseline'	array (L,)	float32	mV	
				Pulse baseline computed from the beginning of the pulse.
'pre_pulse_length'	scalar	float64	ns	0
				Pulse length not used in the beginning of a waveform for coincidence pulse searching.
'procid'	scalar	string		
				Process id. (ex: [12345])
'prompt_frac_TTns'	array (L,)	float32		
				Ratio between the pulse area of the first TT ns and the total pulse area. TT=250,500,750,1000
'random_pulse_areas_post_TTus'	array (M,C)	float32	phe	0
				Pulse area of TT us after a random time. TT=100,50,20,10.
'random_pulse_areas_pre_TTus'	array (M,C)	float32	phe	0
				Pulse area of TT us before a random time. TT=100,50,20,10.
'random_pulse_times'	array (M,C)	float64	ns	nan
				A random time.
'sample_size'	scalar	float64	ns	4
				Aample size of a waveform.
'skimfactor'	scalar	int64		1
				Ratio between the number of all computed pulses and the number of all recorded pulses.
'sphe_size'	array (C,)	float64	mV ns	inf
				Pulse area of a single photo electron in each channel.
'suppress_last_NSamples'	scalar	int32		450
				Number of samples not recorded in the end of a waveform.
				Continued on next page

RQ name	shape	type	unit	default
'times'	array (L,)	float64	ns	
				Pulse start time (since LZ_EPOCH_DATETIME).
'trigvals'	array (L,)	float32	mV	nan
				Pulse trigger voltage.
'usechannels'	array	int32		[0,2]
				Active channels.
'va'	scalar	float32	kV	
				Voltage of the anode grid.
'vg'	scalar	float32	kV	
				Voltage of the gate grid.
'waveamplitudes'	array (L,)	float32	mV	
				Pulse amplitude.
'waveareas'	array (L,)	float32	mV ns	
				Pulse area.
'waveareas_trim_end'	array (L,)	float32	mV ns	nan
				Pulse area suppressing last 'suppress_last_NSamples' samples to 0.
'waveforms'	list (L,)	float32	mV	nan
				Waveform.
'wavelens'	array (L,W)	float32	ns	
				Pulse length.
'window_width'	scalar	float64	ns	1500
				Window size of coincidence pulse searching.
'wtime'	array (L,)	float32	ns	nan
				Pulse height(h_i) weighted average of time(t_i). $\bar{t} = \sum h_i t_i / \sum h_i$.
'wtimeN'	array (L,)	float32	ns ^N	nan
				$\sum h_i (t_i - \bar{t})^N / \sum h_i$. N=2,3,4.

L: number of all computed pulses.

N: number of coincidence pulses.

M: number of random pulses.

C: number of channels.

W: number of samples in a waveform.

F: number of files in a dataset.

Continued on next page

RQ name	shape	type	unit	default
LZ_EPOCH_DATETIME	2015, Jan, 1st, 00 : 00 : 00.			
phe	average photo electron area.			

Table F.1: RQ list

Appendix G

Abbreviations

This chapter summarize the abbreviations that occurs in this thesis.

- #: counts of
- CW: Coincidence Window Size
- ER: Electron Recoil (event)
- LUX: Large Underground Xenon experiment
- LZ: LUX-ZEPLIN experiment
- NR: Nuclear Recoil (event)
- PMT: Photomultiplier Tubes
- PostTW: Post Threshold Window Size
- PreTW: Pre Threshold Window Size
- RQ: Reduce Quantity of a pulse
- S1: primary Scintillation light
- S2: secondary Scintillation light
- TPC: Time Projection Chamber (detector)
- WIMP: Weak Interaction Massive Particle

thesis

Bibliography

- [1] S. Tavernier, “Interactions of Particles in Matter”, in *Experimental techniques in nuclear and particle physics* (Springer Berlin Heidelberg, Berlin, Heidelberg, 2010), pp. 23–53.
- [2] C. J. S. Z. M. A. Berger M.J. and J Chang, *ESTAR, PSTAR, and ASTAR: Computer Programs for Calculating Stopping-Power and Range Tables for Electrons, Protons, and Helium Ions (version 1.2.3) [Online]*, National Institute of Standards and Technology, Gaithersburg, MD., 2005.
- [3] I. T. Steinberger and U. Asaf, “Band-Structure Parameters of Solid and Liquid Xenon”, *Physical Review B* **8**, 914 (1973).
- [4] M. H. Reilly, “Band structure, deformation potentials, and exciton states in solid xenon”, *Journal of Physics and Chemistry of Solids* **28**, 2067 (1967).
- [5] B. Feuerbacher and B. Fitton, “Experimental Investigation of Photoemission from Satellite Surface Materials”, *Journal of Applied Physics* **43**, 1563 (1972).
- [6] C. M. B. Monteiro et al., “Secondary scintillation yield in pure xenon”, *Journal of Instrumentation* **2**, P05001 (2007).
- [7] J. W. Keto, R. E. Gleason, and G. K. Walters, “Production Mechanisms and Radiative Lifetimes of Argon and Xenon Molecules Emitting in the Ultraviolet”, *Physical Review Letters* **33**, 1365 (1974).
- [8] A. Hitachi et al., “Effect of ionization density on the time dependence of luminescence from liquid argon and xenon”, *Physical Review B* **27**, 5279 (1983).
- [9] D. S. Akerib et al., “Results from a Search for Dark Matter in the Complete LUX Exposure”, *Physical Review Letters* **118**, 021303 (2017).
- [10] D. Akerib et al., “FPGA-based trigger system for the LUX dark matter experiment”, *Nuclear Instruments and Methods in Physics Research Section A: Accelerators, Spectrometers, Detectors and Associated Equipment* **818**, 57 (2016).
- [11] D. Akerib et al., “3D modeling of electric fields in the LUX detector”, *Journal of Instrumentation* **12**, P11022 (2017).

- [12] G. Bertone, D. Hooper, and J. Silk, “Particle dark matter: evidence, candidates and constraints”, *Physics Reports* **405**, 279 (2005).
- [13] M. Roos, “Dark Matter: The evidence from astronomy, astrophysics and cosmology”, (2010).
- [14] S. Dodelson, *Modern Cosmology* (Elsevier, 2003).
- [15] K. Olive, “Review of Particle Physics”, *Chinese Physics C* **38**, 090001 (2014).
- [16] S. Burles and D. Tytler, “The Deuterium Abundance toward Q1937 α 1009”, *The Astrophysical Journal* **499**, 699 (1998).
- [17] S. Burles, K. M. Nollett, and M. S. Turner, “What is the big-bang-nucleosynthesis prediction for the baryon density and how reliable is it?”, *Physical Review D* **63**, 063512 (2001).
- [18] N. Jarosik et al., “SEVEN-YEAR WILKINSON MICROWAVE ANISOTROPY PROBE (WMAP) OBSERVATIONS: SKY MAPS, SYSTEMATIC ERRORS, AND BASIC RESULTS”, *The Astrophysical Journal Supplement Series* **192**, 14 (2011).
- [19] J. a. Peacock, “Large-scale structure and matter in the Universe”, *Philosophical Transactions of the Royal Society A: Mathematical, Physical and Engineering Sciences* **361**, 2479 (2003).
- [20] K. G. Begeman, A. H. Broeils, and R. H. Sanders, “Extended rotation curves of spiral galaxies: dark haloes and modified dynamics”, *Monthly Notices of the Royal Astronomical Society* **249**, 523 (1991).
- [21] J. b. Oort, “The force exerted by the stellar system in the direction perpendicular to the galactic plane and some related problems”, *Astronomische Nachrichten* **6**, 249 (1932).
- [22] F. Zwicky, “Die Rotverschiebung von extragalaktischen Nebeln”, *Helvetica Physica Acta* **6**, 110 (1933).
- [23] J. F. Navarro, C. S. Frenk, and S. D. M. White, “The Structure of Cold Dark Matter Halos”, *The Astrophysical Journal* **462**, 563 (1996).
- [24] J. F. Navarro, C. S. Frenk, and S. D. M. White, “A Universal Density Profile from Hierarchical Clustering”, *The Astrophysical Journal* **490**, 493 (1997).
- [25] M. Milgrom, “A modification of the Newtonian dynamics - Implications for galaxies”, *The Astrophysical Journal* **270**, 371 (1983).
- [26] M. Milgrom, “A modification of the Newtonian dynamics as a possible alternative to the hidden mass hypothesis”, *The Astrophysical Journal* **270**, 365 (1983).
- [27] M. Milgrom, “A Modification of the Newtonian Dynamics - Implications for Galaxy Systems”, *The Astrophysical Journal* **270**, 384 (1983).
- [28] B. Famaey and S. S. McGaugh, “Modified Newtonian Dynamics (MOND): Observational Phenomenology and Relativistic Extensions”, *Living Reviews in Relativity* **15**, 10 (2012).